Materials Horizons

ROYAL SOCIETY OF CHEMISTRY

COMMUNICATION

View Article Online
View Journal

Cite this: DOI: 10.1039/d5mh02065d

Fullerene derivative integration controls morphological behaviour and recombination losses in non-fullerene acceptor-based organic solar cells

Apostolos Panagiotopoulos,[a] Kyriakos Almpanidis,[b] Esther Y-H. Hung,[cd] Nikolaos Lempesis,*[e] Weidong Xu,[f] George Perrakis,[g] Sandra Jenatsch,[h] Levon Abelian,[i] Stoichko Dimitrov,[i] Dimitar Kutsarov,[a] Ehsan Rezaee,[a] Benjamin M. Gallant,[jk] Vlad Stolojan,[a] Konstantinos Petridis,[l] Samuel D. Stranks,[f] Henry J. Snaith,[d] George Kakavelakis*[l] and S. Ravi P. Silva*[ab]

Received 30th October 2025,
Accepted 9th December 2025

DOI: 10.1039/d5mh02065d

rsc.li/materials-horizons

The complex and varied relationship found in intermolecular interactions within the photo-active layers plays a decisive role in determining the photovoltaic energy conversion and overall device performance of organic solar cells (OSCs). Among different approaches, the ternary blend strategy serves as an effective technique to control the morphology within the active layer in OSCs. In this work, PM6:L8-BO is used as the main host system (binary) while the fullerene molecules $PC_{61}BM$ and PCBC6 are introduced to form ternary OSCs. The results highlight the important role of fullerenes in enhancing the performance of binary non-fullerene acceptor-based cells by suppressing trap-assisted recombination and optimizing the active layer morphology. The improved film phase microstructure, enabled by fullerene derivatives with higher lowest unoccupied molecular orbital (LUMO) energy levels in comparison to the host acceptor (L8-BO), facilitates more efficient charge collection and reduced non-radiative recombination. This results in an increase in the fill factor (FF) and open circuit voltage (V_{oc}) in the ternary OSCs. Consequently, power conversion efficiencies (PCEs) of binary OSCs were increased from 17.28% to 18.10% and 18.38% for the $PC_{61}BM$- and PCBC6-based ternary OSCs, respectively. Furthermore, the addition of the fullerene molecules in the active layer provided the devices with enhanced long-term photo and thermal stability. The ternary OSCs demonstrated degradation pathways distinct from those of binary cells (ISOS-L1-I and ISOS-D2-I protocols), as identified through *in situ* ultraviolet-visible (UV-Vis) absorption and Raman spectroscopy. Molecular dynamics (MD) simulations, for the first time, reveal the significant role of fullerene molecules as morphology regulators in non-fullerene acceptor (NFA)-based systems. Their presence ensures improved dispersion of blend components and promotes more uniform and isotropic thermal and mechanical behaviour. Finally, mini-modules with active areas of 3.8 cm^2 were fabricated, achieving PCEs of 12.90%, 13.32%, and 13.70% for the binary and ternary cells using $PC_{61}BM$-and PCBC6-based ternary cells, respectively. Our results demonstrate that regulation of the morphology of the photo-active layer in OSCs through fullerene incorporation reduces the non-radiative energy loss pathways, enabling high-efficiency, stable and scalable OSCs.

New concepts

Fullerenes have traditionally been used as the main electron-accepting materials in organic solar cells, achieving efficiencies of up to 10%. Here, we introduce a new role for fullerenes—not as primary active components, but as multifunctional additives in high-performance non-fullerene acceptor (NFA) systems. Rather than extending absorption or facilitating energy level alignment, fullerene additives reduce defects, lower energy losses, and stabilize nanoscale packing without compromising current generation. This overlooked functionality allows them to simultaneously enhance efficiency, extend device stability, and support scalable processing. Through a combination of spectroscopy, device studies, and molecular simulations, we show for the first time that fullerenes smooth blend morphology and promote uniform mechanical behaviour, helping devices resist accelerated degradation. More broadly, this work reframes fullerenes as universal stabilizers for efficient, stable, and industrially viable next-generation solar technologies.

[a] *Advanced Technology Institute, School of Computer Science and Electronic Engineering, University of Surrey, Guildford, UK. E-mail: s.silva@surrey.ac.uk*
[b] *Institute for Sustainability, University of Surrey, UK*
[c] *MAX IV Laboratory, Lund University, P.O. Box 118, Lund, SE-22100, Sweden*
[d] *Clarendon Laboratory, Department of Physics, University of Oxford, Oxford, OX1 3PU, UK*
[e] *Laboratory of Physical Chemistry, Department of Chemistry, University of Ioannina, Ioannina 45110, Greece. E-mail: nlempesis@uoi.gr*
[f] *Department of Chemical Engineering and Biotechnology, University of Cambridge, Philippa Fawcett Drive, Cambridge CB3 0AS, UK*
[g] *Institute of Electronic Structure and Laser (IESL), Foundation for Research and Technology – Hellas (FORTH), 70013 Heraklion, Crete, Greece*
[h] *Fluxim AG, Katharina-Sulzer-Platz 2, 8406 Winterthur, Switzerland*
[i] *School of Physical and Chemical Sciences, Queen Mary University of London, London E1 4NS, UK*
[j] *School of Chemistry, University of Birmingham, Edgbaston, Birmingham, B15 2TT, UK*
[k] *Department of Solution-Processing of Hybrid Materials and Devices Helmholtz-Zentrum Berlin für Materialien und Energie GmbH, Kekuléstraße 5, 12489 Berlin, Germany*
[l] *Department of Electronic Engineering, School of Engineering, Hellenic Mediterranean University, Romanou 3, Chalepa, Chania, Crete, Greece. E-mail: kakavelakis@hmu.gr*

Introduction

Organic solar cells (OSCs) have attracted considerable attention, due to their unique features including low cost, mechanical flexibility, high power-per-weight (PPW) and scalability.[1–18] The use of optimized materials and sophisticated device engineering has resulted in a certified power conversion efficiency (PCE) of over 19% for single-junction bulk heterojunction (BHJ) OSCs.[19,20] Although the advent of non-fullerene acceptors (NFAs) has enabled performance improvements beyond the limitations of fullerene-based OSCs, several critical challenges must still be addressed to ensure continued progress and commercial deployment.[21] Recent findings highlight that the morphology of the photo-active layer is a critical parameter, influencing both the performance and stability of OSCs.[21–24] Despite advances in the chemical design and synthesis of the donor and acceptor materials, non-geminate recombination losses, particularly trap-assisted charge recombination, remain a key limiting factor.[25,26] The persistence and formation of electronic trap states (either intrinsic or induced) present a major obstacle towards high PCEs. Specifically, these traps facilitate the recombination of free carriers, affecting key photovoltaic parameters, mainly the open-circuit voltage (V_{oc}) and fill factor (FF).[27–29] More critically, they can initiate degradation pathways by generating localized heating and promoting morphological or chemical instabilities.[30] Minimizing non-geminate recombination could therefore significantly improve both the performance and stability of OSCs.[31,32]

To date, various optimization strategies have been employed to suppress non-geminate recombination processes, including careful selection of solvents and additives, incorporation of a third component into the photo-active blend, interface engineering, and post-treatment methodologies.[33–38] Among these, the addition of a third component (either a second donor or acceptor) into the BHJ photo-active layer has emerged as a particular promising strategy. This approach can extend the absorption spectra of the BHJ, regulate energy levels, enhance crystallinity and phase separation, and thus, improve charge transport and collection.[31,38–45] The ternary approach in which a lower bandgap NFA is integrated into a fullerene-free binary host BHJ system has attracted considerable interest as this leads to an improved absorption profile of the photo-active layer and, therefore, enhanced device short-circuit current density (J_{sc}).[23,46–51] The use of two NFAs with similar chemical structures can also promote beneficial material intermixing leading to the formation of homogeneous acceptor phases, while still preserving favourable film morphology, ensuring that the FF of the respective OSCs remains intact.[52,53] However, a commonly observed drawback of adding a lower bandgap NFA as a third component is the reduction in V_{oc} that inevitably reduces the PCE.[54–56] To overcome these challenges, recent studies have proposed a novel strategy to increase the V_{oc}. This approach utilizes a guest NFA with a higher lowest unoccupied molecular orbital (LUMO) energy than that of the host NFA-based acceptor in the binary host BHJ system, resulting in a higher V_{oc}.[49,57,58] The favourable interaction between the host and guest acceptors, combined with the guest's ability to adapt to the aggregation behaviour of the host NFA, facilitates improvements in both FF and J_{sc}.[57] Although NFAs have demonstrated clear advantages over fullerene derivatives, particularly as guest electron acceptors for enhancing photon harvesting in the near-infrared region (NIR), the complex morphology of NFA-based ternary OSCs remains an acute challenge to fine tuning the active layer's morphology and thus minimising trap-assisted recombination.[59] Optimization strategies must simultaneously address molecular miscibility and electronic characteristics. Moreover, as NFAs are primarily designed for operation in the NIR region, further chemical engineering is required to enhance absorption capabilities in the higher energy photon (300–700 nm) wavelength range.

On the other hand, fullerenes have historically served as primary acceptors in fullerene-based systems.[60] Generally, fullerene molecules exhibit isotropic electron transport properties, high electron affinity and significant electron mobility attributed to their distinctive spherical fully conjugated structure.[61–63] In addition, fullerene-based compounds show excellent miscibility with the majority of the highly efficient donor materials, and thus facile incorporation of fullerene derivatives into the binary host system has proven an effective strategy to modify photo-active layer morphology and enhance the device performance.[64] Furthermore, adding a suitable fullerene acceptor to form a ternary donor–acceptor–acceptor (D:A:A) blend can tune the energetic alignment of the HOMO–LUMO levels in the active layer, thereby improving charge transfer properties.[65,66] In particular, the fullerene acceptor $PC_{71}BM$ has been demonstrated to significantly improve charge transport and energy transfer in binary systems (full chemical names can be found in the SI section). The addition of 20% of $PC_{71}BM$ (by weight ratio relative to the donor material PM6) has been reported to enhance the performance of PM6:Y6 blends.[67] Similarly, $PC_{71}BM$ can influence the morphology of binary (PM6:L8-BO) active layers, with energy transfer identified as the main working mechanism for these ternary systems.[66] Several reports suggest that the incorporation of fullerene acceptors could enhance the performance of binary NFA-based systems by tuning the energetic alignment or improving the charge transfer characteristics of the devices.[63,64,66,68] However, the interfacial and morphological behaviour of the photo-active layer constitutions (fullerene derivative-based/NFA-ternary OSCs) under illumination and thermal stress remains poorly studied and understood.

In this work, we demonstrate the effect on the performance and stability of two fullerene-based derivative electron acceptors, $PC_{61}BM$ and PCBC6, as the third component in the binary host system consisting of PM6 and L8-BO. The choice of $PC_{61}BM$ and PCBC6 as the third components was based on their distinct advantages.[69] In particular, PCBC6 offers higher solubility in nonpolar solvents, due to its long alkyl chain group, resulting in improved thin film uniformity and smoothness. While PCBC6 has been successfully employed as an electron transport layer in perovskite solar cells, it has not yet been demonstrated as a guest acceptor in ternary OSCs.[69] The

results underscore the crucial role of fullerenes in enhancing the performance of binary NFA-based OSCs. By suppressing trap-assisted recombination and optimizing film morphology, fullerenes enable more efficient charge transfer/collection and thus device operation. The optimized morphology, together with the shallower LUMO levels of the fullerene derivatives relative to the host acceptor, enables more efficient charge collection, thereby enhancing both the FF and V_{oc} in the ternary OSCs. Consequently, the PCE of the binary reference system of 17.28% was increased to 18.10% and 18.38% upon incorporation of $PC_{61}BM$ and PCBC6, respectively, into the ternary blends. Beyond efficiency improvements, the introduction of fullerene molecules markedly prolonged the long-term photo- and thermal stability of the devices. Distinct degradation pathways were observed in the ternary OSCs compared with their binary counterparts, as evidenced by *in situ* UV-Vis absorption and Raman spectroscopic analyses. Moreover, molecular dynamics simulations, reported here for the first time in this context, demonstrated the pivotal role of fullerenes as morphological regulators in NFA-based systems, promoting superior dispersion of the active-layer constituents and yielding more homogeneous and isotropic thermal and mechanical properties. Finally, the scalability of the ternary strategy was validated through the fabrication of mini-modules with an active area of 3.8 cm^2, achieving PCEs of 12.90% for the binary device and 13.32% and 13.70% for the ternary devices incorporating $PC_{61}BM$ and PCBC6, respectively.

Experimental

Materials

All chemicals used in this paper were obtained commercially and used without further purification. The traditional hole conductive polymer poly(3,4-ethylenedioxythiophene):poly(styrenesulfonate) (PEDOT:PSS Al4083) was obtained from (Ossila, UK). The polymer donor poly[(2,6-(4,8-bis(5-(2-ethylhexyl-3-fluoro)thiophen-2-yl)-benzo[1,2-*b*:4,5-*b*′]dithiophene))-*alt*-(5,5-(1′,3′-di-2-thienyl-5′,7′-bis(2-ethylhexyl)benzo[1′,2′-*c*:4′,5′-*c*′]-dithiophene-4,8-dione)] (PM6), the non-fullerene acceptor 2,2′-((2*Z*,2′*Z*)-((12,13-bis(2-ethylhexyl)-3,9-(2-butyloctyl)-12,13dihydro-[1,2,5]thiadiazolo[3,4-*e*]thieno[2″,3″:4′,5′]thieno[2′,3′:4,5]pyrrolo[3,2-*g*]-thieno[2′,3′:4,5]thieno[3,2-*b*]indole-2,10-diyl)bis(methanylylidene))-bis(5,6-difluoro-3-oxo2,3dihydro-1*H*-indene-2,1-diylidene)) dimalononitrile (L8-BO) were purchased from (Solarmer Inc). Both fullerene molecules [6,6]-phenyl-C61-butyric acid methyl ester (PC61BM) and [6,6]-phenyl-C61-butyric acid hexyl ester (PCBC6) were kindly provided by Nano-C Inc. as part of a research collaboration. Furthermore, (poly((2,7-bis(2-ethylhexyl)-1,2,3,6,7,8-hexahydro-1,3,6,8-tetraoxobenzo[*lmn*][3,8]phenanthroline-4,9-diyl)-2,5-thiophenediyl(9,9-bis(3(dimethylamino)propyl)-9*H*-fluorene-2,7-diyl)-2,5-thiophenediyl)) (PNDIT-F3N) was purchased from Solarmer Inc., China and 1,4 diiodobenzene (DIB) were obtained from Sigma-Aldrich, UK and Merck, UK respectively. Chloroform (CF) and methanol (MeOH) were purchased from Thermofisher, UK and Sigma-Aldrich, UK respectively.

Device fabrication

Patterned indium tin oxide (ITO)-coated glass substrates purchased from Huananxianhcheng Ltd (China) (20 mm × 20 mm with a thickness of 1.1 mm and a sheet resistance $< 15\ \Omega\ sq^{-1}$) were first cleaned by sonicating in a 2% v/v Hellmanex in water solution for 20 min. The substrates were then rinsed with deionized water and sonicated in water for a further 15 min. Thereafter, substrates were sequentially cleaned in acetone, 2-propanol, and methanol in an ultrasonic bath at ∼40 °C for 15 min each and blow-dried with nitrogen. Before coating the substrates were subjected to an UV-Ozone process (Jetlight Company In. MODEL 24) for 15 min before fabrication. On top of the precleaned substrates an ∼25-nm-thick PEDOT:PSS thin film was deposited onto the indium tin oxide surface by spin-coating and baked at 150 °C for 15 min. The solutions of PM6:L8-BO (1 : 1.2 w/w, 16.5 mg mL^{-1} in total), PM6:L8-BO:$PC_{61}BM$ (1 : 1.1 : 0.1 w/w, 16.5 mg mL^{-1} in total) and PM6:L8-BO:PCBC6 (1 : 1.0 : 0.2 w/w, 16.5 mg ml^{-1} in total) in CF with 1,4-DIB as a solid additive (the content of 1,4-DIB is 50% of the total mass of donor and acceptor) were spin-coated in a nitrogen filled glove box on top of the PEDOT:PSS layer. The photo-active layer thickness of the devices was ∼100 nm for the three different blends. The prepared films were treated with thermal annealing at 85 °C for 5 min. After cooling to room temperature, a ∼5-nm-thick PNDIT-F3N (0.5 mg mL^{-1} in MeOH with 0.5% acetic acid, v/v) was spin-coated on the top of the active layer. Then, the samples were transferred into the evaporating chamber Angstrom EvoVac system inside the glovebox, and a 100-nm-thick silver (Ag) layer was thermally evaporated on the PNDIT-F3N layer.

For the fabrication of mini-modules, the glass-ITO substrates were first P1 scribed (total laser power of 1.0 W cm^{-2}) using a HyperRapid NXT laser from Coherent generating picosecond pulses at 532 nm. After cleaning and deposition of all functional layers, the samples were subjected to a P2 scribe (total laser power of 3.0 W cm^{-2}) to expose the ITO. To accomplish a monolithic serial connection between the individual subcells, the Ag electrode was evaporated thermally on top of the complete device area and then P3 patterned (total laser power of 3.5 W cm^{-2}) in order to separate the top Ag contacts. Finally, a P4 cut removing all layers including the ITO was made. This resulted in the formation of a mini-module consisting of 4 individual cells (0.95 cm^2 active area per cell, 3.8 cm^2 in total for the mini module), which was electrically isolated from the surrounding area on the substrate.

Current (*I*)–voltage (*V*) characteristics

I–V characteristics of the fabricated solar cells were evaluated using an Enlitech SS-F5-3A (Class 3A) solar simulator with a Keysight 2901A source measure unit acting as the electrical load. The calibration of the simulator was carried out using a KG-5 filtered Si diode. A mask with 0.09 cm^2 aperture area was used to define the active area of the device. The physical area of the device (the overlap between the top and bottom electrodes) was 0.25 cm^2. For the measurement of mini-modules, an exact

aperture area of 3.8 cm^2 (confirmed with a digital microscope) was used. All devices were measured with a light intensity of 100 mW cm^{-2} (AM1.5G), calibrated using a reference cell purchased from Fraunhofer ISE CalLab (ISE001/013-2018).

External quantum efficiency (EQE)

EQE measurements of the fabricated devices were carried out using a Bentham PVE300 system. All measurements were carried out under ambient conditions. The monochromatic light intensity was calibrated by a traceable silicon reference detector (300–1100 nm) from the national metrology institute (NMI). All devices were measured without any encapsulation under ambient conditions at a temperature of ~25 °C and a relative humidity of 30–35%. For each device, a 0.16 cm^2 mask was used during the measurement to ensure that the probing beam (size is 2.2 mm × 2.2 mm) was fully inside the electrode area.

Electroluminescence (EL) quantum efficiency measurement

The EL quantum efficiency measurement was performed by recording absolute EL spectra while simultaneously conducting a *J–V* scan in the dark. A home-built system was used, comprising an integrating sphere (Labsphere), a spectrograph (HRS 500, Teledyne), and a CCD camera (PIXIS:1024BR_eXcelon, Teledyne) for EL spectrum collection. A source measure unit (Keithley 2400) applied voltage and recorded current. A custom Python script synchronized the spectrometer control software (LightField, Teledyne Princeton Instruments) with the Keithley for system control and data acquisition. Spectrometer wavelength calibration was performed using a mercury light source (PI Mercury, Teledyne Princeton Instruments), and absolute photon flux calibration was done using a halogen light source (HL-3 plus-CAL-INT, Ocean Optics) with known irradiance. All measurements were carried out at a scan rate of 10 mV s^{-1}, from 0.8 V to 1.5 V, in 0.05 V steps.

Transient absorption spectroscopy

Solstice regenerative amplifier (Newport corporation) was used for pump and probe light pulse generation. The Solstice output was 1 KHz and 800 nm. A part of the output beam was used for sample excitation, and ND filters controlled the pump intensity. A transient absorption spectrometer (Helios, Ultrafast systems) with two detection cameras was used for signal detection, where one of the cameras was used for signal detection while the other was used for tracking probe light fluctuations. The probe beam was generated in the spectrometer in a sapphire plate. The time delay in the experiment was achieved *via* a high precision delay stage, changing the pump beam pathway length. Thin films of PM6:L8-BO:fullerene were prepared on microscope glass slides according to the device fabrication procedures and kept under a positive inert, N_2, environment during experiments. No material degradation was observed during experiments. Data was analysed using Origin. For fitting of kinetics, the Origin embedded function titled FitConvExp3P10 was used, convoluting the Gaussian peak function with three exponential functions.

Photo-CELIV

Photo-CELIV measurements were performed with the commercial Paios system (Fluxim AG) employing a white LED with varied intensity and employing a ramp rate of 100 V ms^{-1}.

Thermal/light MMPT stability test

For the light stability tests, samples were illuminated in the nitrogen chamber at room temperature, with a light intensity equivalent to 1-Sun (100 mW cm^{-2}) using an LED 6500 K light source and tracking the maximum power point condition. For the thermal test, the samples were tested under dark conditions at 85 °C inside a nitrogen glovebox.

Ultraviolet-visible (UV-Vis) absorption

The absorption spectra were obtained using a Varian Cary 5000 UV-Vis-NIR spectrophotometer.

Atomic force microscopy (AFM)

AFM images were obtained using Bruker Dimension Edge in tapping mode with a scanning area size of 10 μm × 10 μm for each sample.

Raman spectroscopy

RAMAN experiments were conducted using a Wasatch WP532-C-SR-S-50 spectrometer and 532 nm, 100 mW, CW laser. The samples were illuminated by a Bentham IL1_150 quartz halogen lamp (150 W), trained onto the sample at approximately 45 degrees (so that the Raman laser could be set up perpendicularly), with the power supply at 6.3 A, producing light intensity at the sample position of ~0.3 W, three times the AM1.5 G solar spectrum of 0.1 W cm^{-2}. The absorption experiments utilized a Shimadzu UV 3600 Plus UV-Vis-NIR spectrophotometer. The samples were unencapsulated and the experiment was conducted in ambient air.

Grazing-incidence wide-angle X-ray scattering (GIWAXS)

GIWAXS measurements were performed on a Rigaku SmartLab X-ray diffractometer with a 3 kW Cu X-ray source (1.54060 Å, 8.04 keV) in parallel beam configuration with 0.5° pinhole optics, a 1° in-plane parallel slit collimator and 0.3° long collimator attachments. Scattering was collected with a HyPix-3000 2D hybrid pixel array detector, with a 65 mm sample-to-detector-distance (SDD), with incidence angles between 0.12 and 0.16° in order to maximize the scattering intensity from the samples. For each measurement, the detector goniometer arm was rotated through 2θ angles from 0° to 40° in 1° steps, with 6 min acquisition at each position, with detector images then remapped into *Q*-space and combined together. All data reduction was performed using scripts based on the PyFAI and pygix libraries.[70,71]

Results and discussion

Chemical structures, optoelectronic and morphological characteristics

The chemical structures of the donor polymer PM6 and the acceptors L8-BO, PCBC6, and $PC_{61}BM$ are shown in the SI, Fig. S1. The normalized ultraviolet-visible (UV-Vis) absorbance spectra of thin films obtained with these materials are shown in Fig. 1(a). L8-BO demonstrates a broad absorption from 400 to 880 nm, complementary to that of the donor material PM6, which exhibits an absorption profile between 300 and 680 nm. On the other hand, the absorption profiles of the fullerenes span ~680 to 300 nm and could additionally contribute to an extended light absorption. However, previous studies show that the main function of fullerenes in binary D:A systems is to facilitate efficient exciton dissociation and consequent charge carrier transport.[25,68,72–75] More specifically, the use of different fullerene molecules can significantly influence molecular packing within the BHJ, suppress recombination and minimally contribute to carrier generation (<5% contribution to photocurrent, while polymer/NFA dominate carrier generation).

Atomic force microscopy (AFM) was used to determine the surface topography of the binary and ternary blend films (all characterization studies, including AFM, presented in the main text correspond to the optimized ternary blends, for more details see the photovoltaic performance section). Notably, all blends presented well-distributed film topologies, indicating good miscibility between the blend components. Fig. 1(b) shows the AFM height images, while Fig. 1(c) presents the corresponding surface height histograms as extracted from the corresponding images. The AFM height images reveal root-mean-square surface roughness (R_q) values of 1.34 ± 0.09 nm for the binary and lower R_q values of 1.09 ± 0.06 nm and 1.12 ± 0.07 nm after the incorporation of $PC_{61}BM$ and PCBC6, respectively. The slightly different R_q values for the ternary cells incorporating the two fullerene derivatives may arise from the different chemical structures (unmodified fullerene $PC_{61}BM$ *vs.* functionalized fullerene derivative PCBC6). Overall, the results suggest that the optimal amount of fullerene incorporated in the active layer could lead to a smoother film, indicating a more uniform surface morphology.

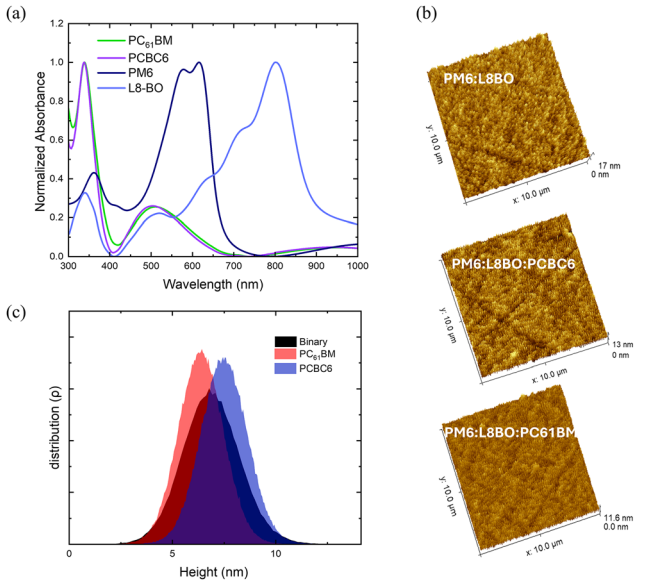

Fig. 1 (a) Normalized absorbance spectra of PM6, L8-BO, PCBC6 and $PC_{61}BM$, (b) AFM images of the binary and ternary blends and (c) surface height histograms of various blends calculated from the corresponding AFM height images.

GIWAXS analysis

To assess the influence of the guest acceptor on crystalline morphology, 2D grazing-incidence wide-angle X-ray scattering (GIWAXS) measurements were performed (Fig. 2). All blends exhibit both lamellar (100) and π–π stacking (010) features at $Q \sim 0.3$ Å^{-1} and 1.55 Å^{-1} respectively, in agreement with previous reports (Fig. 2(a–c)).[76] Alongside the primary peaks ($Q \sim 0.3$ Å^{-1}) from the PM6 donor, a very weak, diffuse feature centred at $Q_{xy} \sim 0.38$ Å^{-1} is tentatively assigned to the $(11\bar{1})$ peak of the L8-BO acceptor (Fig. 2(d)).[77] The intensity ratio of the out-of-plane π–π to in-plane lamellar peaks decreases from 1.00 in the binary blend to 0.96 and 0.91 with the addition of $PC_{61}BM$ and PCBC6, respectively, indicating an increased ordering of the lamellar stacking.[78] Quantitative analysis of the 1D linecuts (Fig. 2(d)) reveals distinct acceptor-dependent packing modifications. Whilst the π–π stacking peak at 1.566 Å^{-1} remains the same upon the addition of PCBC6, this increases slightly to 1.570 Å^{-1} with $PC_{61}BM$, consistent with a modest increase π–π interaction strength.[79] The tighter π–π packing with $PC_{61}BM$ enhances charge transport along the conjugated backbone, consistent with known benefits of face-on orientation for both hole and electron mobility.[80] On the other hand, the in-plane (100) lamellar peak remains nearly unchanged for the ternary containing $PC_{61}BM$ (0.303 Å^{-1} and 0.304 Å^{-1} for the binary and ternary with $PC_{61}BM$), whereas a pronounced reduction to 0.258 Å^{-1} is observed upon PCBC6 incorporation, corresponding to a *d*-spacing expansion from ~20.7 Å to ~24.3 Å. The substantial lamellar dilation upon PCBC6 addition contrasts with this fullerene's modest effect and highlights its longer alkyl chain-driven morphological changes.[69] To determine the quality of the crystallisation, the crystalline coherence lengths (CCLs) were estimated by fitting the peaks shown in Fig. 2(d) (Supplementary Note 1). The π–π stacking CCL remains the same 13.03 Å in the binary films and the addition of $PC_{61}BM$-based ternary films, but increases to 13.59 Å with PCBC6, indicating enhanced molecular ordering along this direction for PCBC6-based ternary films only.[81] The lamellar CCLs exhibit more substantial changes, increasing significantly from 52.8 Å in the binary to 53.95 Å and 66.50 Å for the $PC_{61}BM$ and PCBC6-based blends respectively, suggesting that PCBC6 leads to longer range lamellar ordering.[82] $PC_{61}BM$ and PCBC6 may therefore mediate distinct charge transport pathways in the ternary blends. While $PC_{61}BM$ enhances π–π coupling, expected to be beneficial for charge transport, the increased lamellar stacking induced by PCBC6

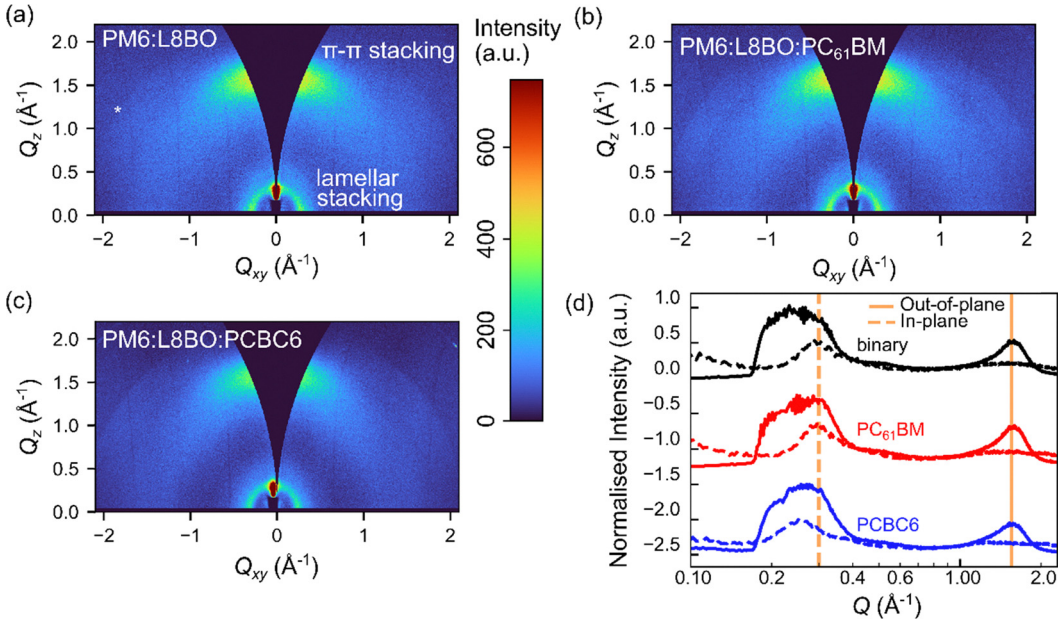

Fig. 2 (a)–(c) 2D GIWAXS patterns for the different blends. The white asterisk indicates the ITO substrate peak. (d) Line cuts of the in-plane and out-of-plane regions, corresponding to the lamellar and π–π stacking, respectively. Vertical dashed and solid orange lines indicate the relative peak shifts of the lamellar and π–π peak, respectively, with respect to that of PM6:L8-BO. The regions used to produce the linecuts are shown in the SI, Note 1.

promotes long-range molecular ordering through its stronger intermolecular interactions, expected to reduce energetic disorder (narrowing trap states) and suppress charge recombination in the resulting OSCs.[80,81,83]

Photovoltaic performance

To correlate structural and morphological changes with photovoltaic device performance, we proceed with device fabrication. For the fabrication of the ternary OSCs, the amount and the ratio of the guest fullerene acceptor relative to the binary host system are essential, as it impacts the optical and electrical properties of the photo-active layer. Herein, optimized PM6:L8-BO binary OSCs were used as the control samples following our previous work.[84] Ternary-based blend devices were fabricated in p–i–n (conventional structure), maintaining the overall donor-to-acceptor D : A ratio as a constant of 1 : 1.2, while the quantity of each fullerene derivative was optimized as shown in the SI, Fig. S2 and S3. The optimal weight ratio for each fullerene derivative was 1.0 : 1.0 : 0.2 for PM6 : L8-BO : PCBC6 and 1.0 : 1.1 : 0.1 for PM6 : L8-BO : $PC_{61}BM$, respectively. The representative current density *versus* voltage (*J*–*V*) curves obtained from the champion individual device for each fullerene derivative are shown in Fig. 3(a), with a summary of the device photovoltaic parameters provided in Table 1.

The PM6:L8-BO-based OSCs demonstrated a maximum PCE of 17.28% on the 0.09 cm^2 active area with a J_{sc} value of 26.44 mA cm^{-2}, a V_{oc} of 0.85 V, a FF of 76.91% and a series resistance (R_s) of 2.40 Ω cm^{-2}, which is among the highest published output device performance for PM6:L8-BO-based OSCs. Moreover, PM6:L8-BO:$PC_{61}BM$-based cells exhibited a maximum PCE of 18.10% with a J_{sc} of 26.55 mA cm^{-2}, a V_{oc} of 0.86 V, a FF of 78% and an R_s of 2.27 Ω cm^{-2}. Remarkably, the PM6:L8-BO:PCBC6-based devices showed a maximum PCE of 18.38% with an increased J_{sc} of 26.85 mA cm^{-2}, a FF of 78.7%, a V_{oc} of 0.87 V and R_s of 2.28 Ω cm^{-2}. As expected, the incorporation of the different fullerene derivatives slightly increases the V_{oc} of the ternary devices compared to their binary counterpart. This is ascribed to the energy offset of the BHJ materials (E_{Donor} HOMO)–($E_{Acceptor}$ LUMO) which is the main factor determining the device V_{oc}.[85] This can be further supported by the higher LUMO energy levels of the guest fullerene acceptors $PC_{61}BM$ and PCBC6 compared to that of L8-BO.[69,86–88] Additionally, the higher V_{oc} of PCBC6 ternary-based devices is due to the shallower LUMO energy level compared to those for $PC_{61}BM$. The higher FF values obtained for both $PC_{61}BM$ and PCBC6 relative to the host binary may be attributed to an improved blend morphology, which helps to suppress the recombination losses and facilitates more efficient charge extraction pathways. In addition, the smaller R_s values for the ternary $PC_{61}BM$ and PCBC6-based blends suggest better interfacial contact with the adjacent layer, consistent with the lower R_q surface roughness values for both ternary blends as obtained by the AFM measurements (Fig. 1(band c)).

To further support the experimental J_{sc} values obtained from the *J*–*V* curves, external quantum efficiency (EQE) measurements were performed to derive the integrated J_{sc} values, as shown in Fig. 3(b). The obtained J_{sc} trend is consistent with that observed in the *J*–*V* data. Moreover, the calculated EQE J_{sc} values presented an average deviation of 6%, which is in good agreement with the values obtained from the *J*–*V* curves. The incorporation of the fullerene component results in a marginal

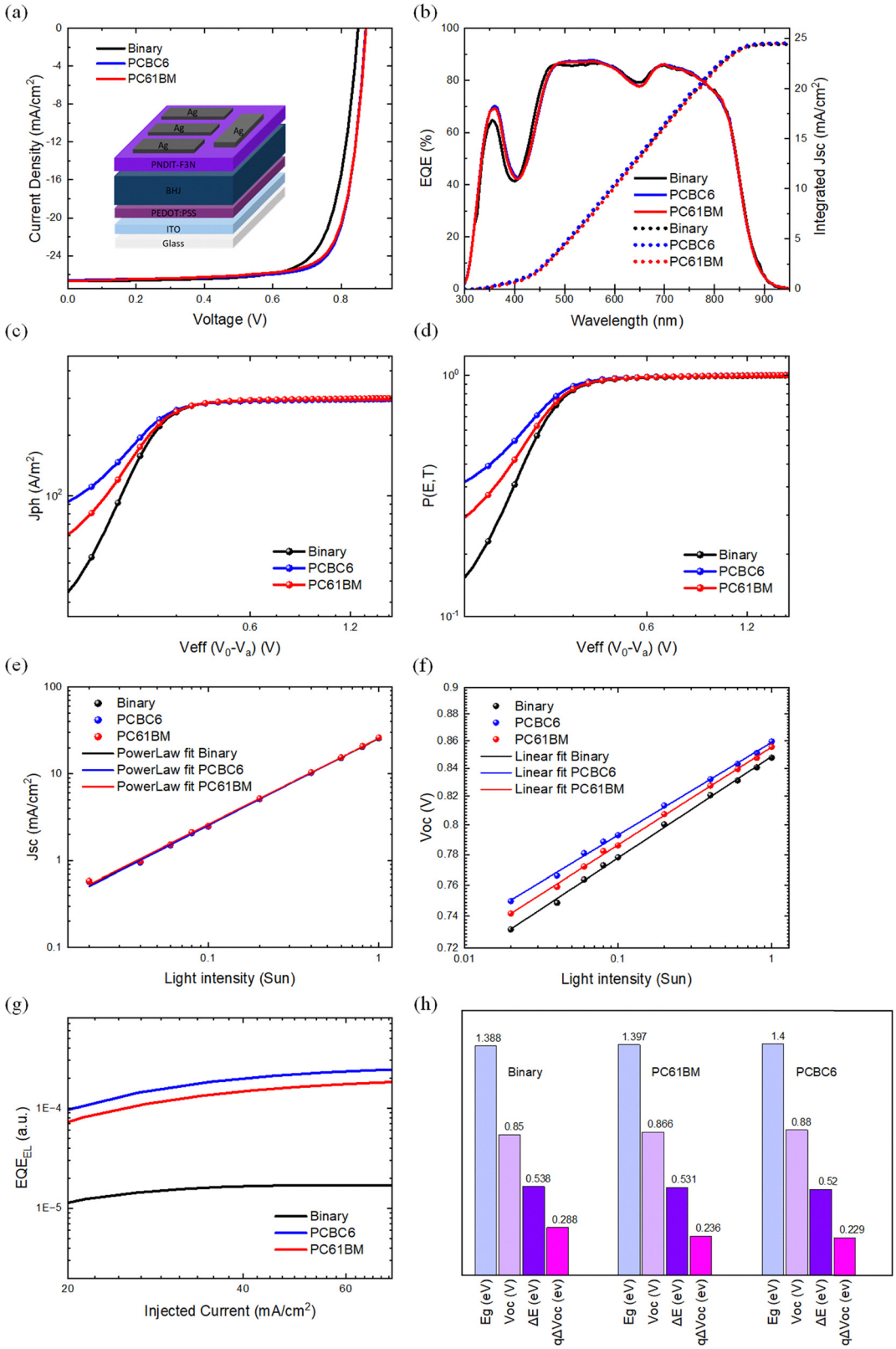

Fig. 3 (a) J–V curves for the champion cells for binary and ternary OSCs with an insert showing the OSC device stack, (b) EQE and integrated J_{sc} of binary and ternary OSCs, (c) photocurrent density (J_{ph}) *versus* effective voltage (V_{eff}) curves of the device, (d) charge collection probabilities P(E, T) curves of the binary and ternary cells, (e) J_{sc} and (f) V_{oc}, *versus* light dependence measurements of the devices based on binary and ternary blends, (g) electroluminescence quantum efficiency of the binary and ternary blends at different injected currents, and (h) voltage loss waterfall chart for each blend system.

Table 1 Summary of characteristic parameters for binary and ternary OSCs extracted from the *J–V* curves

Blend	V_{oc} (V)	J_{sc} (mA cm^{-2})	$J_{sc,EQE}$ (mA cm^{-2})	FF	PCE (%)	R_s (Ω cm^{-2})
PM6:L8-BO	(0.858 ± 0.007)	(25.90 ± 0.57)	24.39	(76.63 ± 0.96)	(17.02 ± 0.20)	(2.52 ± 0.08)
PM6:L8-BO:$PC_{61}BM$	(0.866 ± 0.005)	(26.14 ± 0.36)	24.48	(78.52 ± 0.53)	(17.76 ± 0.21)	(2.29 ± 0.04)
PM6:L8-BO:PCBC6	(0.871 ± 0.002)	(26.43 ± 0.31)	24.52	(78.66 ± 0.60)	(18.11 ± 0.17)	(2.32 ± 0.03)

enhancement in EQE (mainly in the wavelength range of 300–550 nm) compared to the binary host system, as expected considering the contribution of $PC_{61}BM$ and PCBC6 in the UV-Vis absorbance spectra. The effect of the almost unchanged EQE spectra indicates similar charge generation profiles for the binary and the ternary cells, which is further supported by the transient absorption spectroscopy analysis and the charge generation calculations as described later.

Exciton generation rate and charge collection probabilities

To gain better insight into the exciton generation and dissociation processes, the dependence of the photocurrent densities (J_{ph}) of the cells with the different photo-active blends was plotted *versus* the effective voltage (V_{eff}), from which the maximum exciton generation rate (G_{max}) and charge collection probabilities P(E, T) were calculated. J_{ph} is determined as $J_{ph} = J_L - J_D$, where J_L and J_D are the current densities under illumination and dark conditions, respectively. V_{eff} is determined as $V_{eff} = V_0 - V_a$, where V_0 is the voltage at the point of $J_{ph} = 0$, and V_a is the applied bias voltage. Assuming that the saturated current density (J_{sat}) is defined by the total quantity of the absorbed photons and all the photogenerated excitons are dissociated to free charge carriers at higher voltage (>1 V), then G_{max} can be extracted with $J_{sat} = qG_{max}L$.[89,90] The values of G_{max}, as calculated from Fig. 3(c) were 1.631 × 10^{28} s^{-1} m^{-3} (261 A m^{-2}) for the PCBC6-based cells, 1.625 × 10^{28} s^{-1} m^{-3} (260 A m^{-2}) for the $PC_{61}BM$-based cells and 1.612 × 10^{28} s^{-1} m^{-3} (258 A m^{-2}) for the binary-based cells. Fundamentally, the G_{max} is correlated to the maximum absorption of incident photons.[91,92] The almost unchanged values of G_{max} suggest that the overall exciton generation rates of all devices are very similar. Moreover, the charge collection probability $P(E, T)$ can be calculated from the ratio of J_{ph}/J_{sat}.[93] Under short circuit conditions for the binary cells, the control device $P(E, T)$ was calculated to be (97 ± 1%), while the devices based on PCBC6 and $PC_{61}BM$ exhibited values of (98 ± 1%) and (98 ± 1%), respectively, see Fig. 3(d). The increased $P(E, T)$ values of the PCBC6 and $PC_{61}BM$ samples suggest a more efficient charge collection compared to the reference binary cells, which can be further corroborated by the higher FF values as obtained by the *J–V* measurements.

Light dependent *J–V* measurements

To understand the charge recombination process, the dependence of V_{oc} and J_{sc} *versus* the light intensity (P_{light}) was measured.[94] As depicted in Fig. 3(e), the relationship between J_{sc} and P_{light} can be expressed as $J_{sc} \propto P_{light}^{\alpha}$, where α is the slope of the curve. The α values for the devices with PCBC6, $PC_{61}BM$, and the reference binary blend were calculated at 0.997, 0.996 and 0.994, respectively. These results suggest that the α values of all three BHJ blends are almost identical, indicating that the presence of bimolecular recombination is weak in all of them.[94] The charge carrier recombination mechanism of the devices can be further clarified by determining the slope of V_{oc} *versus* the P_{light}, as shown in Fig. 3(f). Typically, under open-circuit conditions, the presence of bimolecular recombination leads to a slope of kT/q, with k representing the Boltzmann constant, T as the temperature in Kelvin, and q as the elementary charge. In contrast, if monomolecular or trap-assisted recombination is the dominant mechanism, a more pronounced dependence of V_{oc} on P_{light} is observed, yielding a slope of $2kT/q$.[95] The devices with PCBC6, $PC_{61}BM$ and binary blends show slopes of 1.210, 1.275 and 1.324 kT/q, respectively. The lower values for PCBC6 and $PC_{61}BM$ compared to the binary cells suggest that their incorporation reduces trap-assisted recombination and therefore leads to an increment on the V_{oc} of the ternary-based cells as also evidenced by the *J–V* data.[27,96]

Voltage–energy losses

Additionally, to elucidate the rise in V_{oc} after the addition of fullerenes as a third component, the total loss ($\Delta E = \Delta V_{oc}$) of the different BHJ blends were calculated according to $\Delta E = E_g - qV_{oc}$, where E_g is the optical band gap estimated from the EQE.[97,98] The E_g values of PM6:L8-BO, PM6:L8-BO:$PC_{61}BM$ and PM6:L8-BO:PCBC6 are 1.388 eV, 1.397 eV and 1.400 eV, respectively. Accordingly, ΔE reduces from 0.538 eV to 0.531 eV and 0.520 eV for PM6:L8-BO, PM6:L8-BO:$PC_{61}BM$ and PM6:L8-BO:PCBC6-based devices, respectively, as shown in Fig. 3(h). It is essential to underscore that electroluminescence external quantum efficiency (EQE_{EL}) is intricately related to the non-radiative V_{oc} loss, as represented by the equation: $q\Delta V_{oc}^{nonrad} = -k_BT\ln(EQE_{EL})$, where k_B is the Boltzmann constant, T is the temperature in Kelvin, and EQE_{EL} denotes the electroluminescence quantum efficiency of the device under dark conditions.[99,100] The EQE_{EL} short-circuit current density is adopted to evaluate the charge recombination characteristics, as illustrated in Fig. 3(g). Thus, the binary-based devices exhibited an EQE_{EL} of 1.34 × 10^{-5} representing a voltage loss of 0.288 V due to non-radiative recombination. On the other hand, the ternary OSCs based on $PC_{61}BM$ and PCBC6 demonstrated higher EQE_{EL} values of 1.16 × 10^{-4} and 1.14 × 10^{-4}, representing voltage losses of 0.236 V and 0.229 V, respectively (Table 2). Our findings suggest that the addition of the fullerene components is crucial for the design of efficient ternary OSC systems, indicating that the introduction of the optimum

Table 2 E_{loss} energy loss of OSCs based on binary and ternary BHJ blends

BHJ	V_{oc} (V)	E_g (eV)	ΔE (eV)	$q\Delta V_{oc}^{nonrad}$ (eV)	EQE_{EL}
PM6:L8-BO	0.850	1.388	0.538	0.288	1.34×10^{-5}
PM6:L8-BO:$PC_{61}BM$	0.866	1.397	0.531	0.236	1.16×10^{-4}
PM6:L8-BO:PCBC6	0.880	1.400	0.520	0.229	1.14×10^{-4}

amount of fullerene molecules serves as a mitigation strategy to reduce non-radiative recombination losses. Notably, the smaller $q\Delta V_{oc}^{nonrad}$ originating from tuning the energy levels offsets between PM6 and L8-BO by the addition of the fullerene molecules, contributes to the reduced total ΔE and the enhancement of V_{oc} of the ternary BHJ OSCs. The results agree with the J_{sc} and V_{oc} light dependent measurements which are consistent with the reduced trap-assisted recombination in the ternary devices compared to the binary cells.

Transient absorption spectroscopy (TAS)

To further investigate exciton generation and validate previous findings, TAS measurements were carried out to investigate the effect of the fullerene derivative addition on the early timescale exciton and charge dynamics in the blended films. For this purpose, L8-BO was excited with 800 nm light pulses (8.4 μJ cm^{-2}). Fig. 4(a) presents the transient absorption signal at 630 nm probing the bleach of the PM6 component. It is evident that all blends have similar excited state dynamics on the sub-nanosecond timescale corresponding to charge transfer from L8-BO to PM6. An exponential fit to the PM6:L8-BO data estimates two-time constants: 0.4 ± 0.1 ps and 15.0 ± 4.0 ps, which are consistent with published data and correspond to two types of charge transfer processes; interfacial charge transfer and exciton diffusion limited charge transfer, respectively.[101] Moreover, the decay of the PM6 bleach signal up to 6 ns as shown in SI, Fig. S4, shows that charge recombination is not influenced by the fullerene derivatives. These results reveal that charge transfer and recombination within the first 6 ns after excitation are independent of the fullerene component but dictated by optimal PM6:L8-BO blend structure and packing on the nanometre length scale,[81] corroborating the observation of insignificant differences in J_{sc} of the devices from the *J–V* curves/EQE and the exciton generation rate calculations.

Charge carrier lifetimes

To obtain additional insight into the operation of the various OSCs, we performed electrochemical impedance spectroscopy (EIS) measurements which provide important insights related to the charge extraction lifetime (τ) and bulk resistances.[102] EIS measurements were performed to examine the transient behaviour in the various OSCs fabricated in this work. Thus, the measurements were obtained, under dark conditions from 1 Hz to 1 MHz, with DC bias equal to the V_{oc} for each device.[103] The Nyquist plots and the fitting model were fitted by using the equivalent circuit model[104,105] shown in Fig. 4(b), while the relevant data for each active layer blend is summarized in Table 3.

The R_e corresponds to electrode resistance (ITO and A_g); R_{int} and C_{int} in parallel correspond to the interface layer's resistance and capacitance, and R_{bhj} and C_{bhj} in parallel correspond to the resistance and capacitance of the bulk heterojunction, respectively. The performance of the OSCs can be correlated by analyzing the R_{int} of the interface layer in conjunction with the average carrier transition lifetime (τ).[105,106] Notably, the PCBC6 and $PC_{61}BM$ ternary-based cells exhibited lower R_{int} values (18.7 Ω and 18.9 Ω) compared to the binary cells which supports our findings regarding the higher FF values obtained from the *J–V* analysis.[27] Additionally, since the only variable is the photo-active layer, the τ values for each blend were calculated based on the equation $\tau = R_{bhj} \cdot C_{bhj}$. The τ values for PCBC6, $PC_{61}BM$ and binary-based cells were calculated as 9.04 μs, 8.82 μs and 8.62 μs respectively. The longer τ values for the PCBC6, $PC_{61}BM$-based OSCs compared to the binary cells indicate reduced trap-assisted recombination, consistent with the light-dependence measurements and charge collection probabilities.[107] Overall, the EIS findings highlight the effect of the PCBC6 and $PC_{61}BM$, which contributes to reduced charge recombination and improved charge extraction to the electrodes compared with the binary, ultimately enhancing the FF and PCE.[108]

Built-in potential, Mott–Schottky analysis

To further confirm the V_{oc} improvement of the ternary systems by the incorporation of the fullerene derivatives, capacitance–voltage (*C–V*) measurements were carried out to probe the built-in potential (V_{bi}) and explore the effective separation of photogenerated carriers for each variation. Generally, it can be presumed that no efficient organic solar cell can exist (exhibiting reasonable FF) with a V_{bi} that is considerably smaller than its device V_{oc} ($V_{bi} < V_{oc}$).[109] In this case, the FF would suffer drastically from the low V_{bi}, since the photogenerated charge carriers must diffuse against the electric field to be collected at the corresponding contacts.[110] For this purpose, the Mott–Schottky equation was used: $1/C^2 = 2(V + V_{bi})/eN_D\varepsilon_s\varepsilon_0$, where V is the bias voltage, N_D is the doping level of the semiconductor, and ε_s and ε_0 are the permittivity of the semiconductor and vacuum, respectively.[111] In this model, the $1/C^2$ scaled linearly with V and the extrapolation to the abscissa yields the V_{bi}. The Mott–Schottky plots for the binary host, PCBC6 and $PC_{61}BM$-based ternary OSCs, as shown in Fig. 4(c). The obtained V_{bi} values were 0.867, 0.893, and 0.882 for the binary host, PCBC6, and $PC_{61}BM$-based ternary OSCs, respectively. The apparent increase in the V_{bi} for the ternary blends is consistent after the addition of the third component and in agreement with the trend of the V_{oc} values obtained from the *J–V* characteristics. These findings also confirm that V_{bi} extracted from the *C–V*

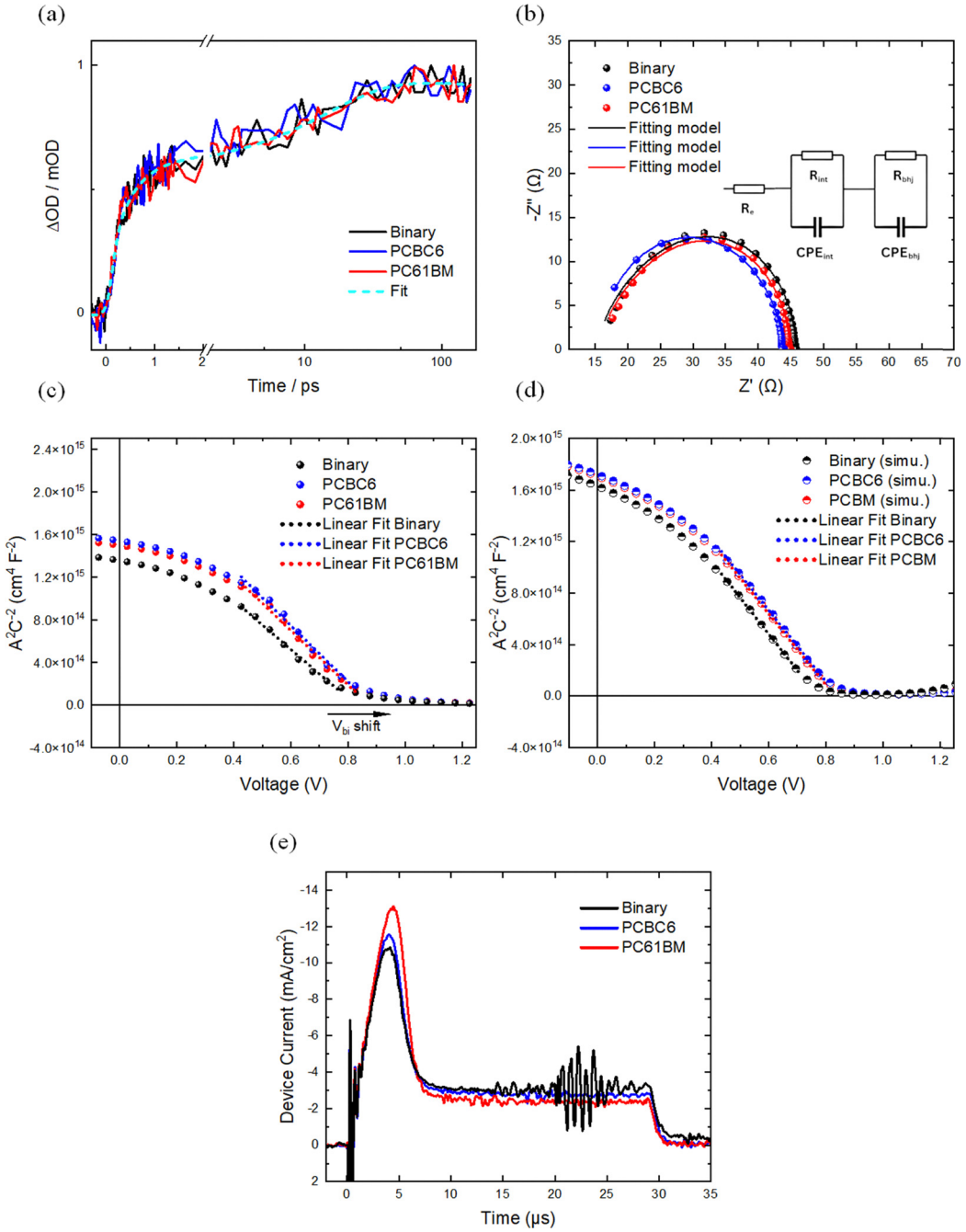

Fig. 4 (a) Transient absorption signal at 630 nm plotted as a function of time, probing the bleach signal of PM6 and excited with 800 nm at L8-BO. The cyan broken line represents a fit to the experimental data using a convolution of Gaussian and three exponential functions, (b) Nyquist plots of the EIS data with the equivalent fitting models for the various OSCs, (c) Mott–Schottky analysis curves under dark conditions for the binary and ternary OSCs, (d) simulated $1/C^2$–V curves for binary and ternary cells, and (e) photo-CELIV transient for representative devices for binary and ternary photo-active layers.

Table 3 Summary of the fitting parameter used to describe the Nyquist plots

BHJ	R_e (Ω)	R_{int} (Ω)	C_{int} (nF)	R_{bhj} (Ω)	C_{bhj} (nF)	τ (μs)
PM6:L8-BO	15.3	19.1	150	11.50	750	8.62
PM6:L8-BO:$PC_{61}BM$	15.5	18.9	115	10.50	840	8.82
PM6:L8-BO:PCBC6	15.2	18.7	87	10.10	895	9.04

characteristics is determined by the internal D:A heterojunction as suggested by the latest evidence in the literature.[112] Consequently, the presence of a stronger electric field in devices with a larger V_{bi} results in an increased V_{oc}[113] as further supported by the voltage-losses measurements, which also yields higher FF values.

We further explore the above findings by interpreting the simulated *C–V* characteristics (see Fig. 4(d)) derived from steady-state device simulations.[114] Specifically, steady-state simulations yielded spatial charge distributions, which were used to numerically construct the $1/C^2$–*V* plots under the quasi-static approximation (see the ''Device Simulations Part A (*C–V*)'' section in the SI).[115] The results showed close agreement with experimental Mott–Schottky diagrams (Fig. 4(c)), exhibiting linear behaviour with applied voltage and similar V_{bi} trends. Notably, the simulated diagrams accurately reproduce the increased V_{bi} values observed for the ternary OSCs compared to the binary device. Our simulations indicate that this enhancement may arise from the shallower effective LUMO levels introduced by the additional fullerene components (slightly shallower for PCBC6 than $PC_{61}BM$; see Table S1, SI),[24,69] further supporting the interpretation that fullerene energetics play a key role in tuning both V_{bi} (Fig. 4(c)) and V_{oc} (Fig. S5(b), SI) in these systems.[112]

Density of extracted charge carriers

Charge transport critically governs OSC performance, particularly in photo-active layers incorporating multiple donors and acceptors. Adverse interactions between the three different materials can suppress charge transport and thus limit the overall device PCE.[116] For this purpose, we also explored the mobility of charge carriers within devices that feature the different BHJ photo-active layers, employing photoinduced charge carrier extraction through linearly increasing voltage (photo-CELIV). The area under the photo-CELIV peak corresponds to the density of extracted charge carriers and depends on the number of carriers initially photogenerated by the light-emitting-diode (LED) pulse. Typically, recombination occurring during the CELIV voltage ramp reduces this integrated charge density relative to the initially generated charges. Hence, a reduced peak area serves as an indicator of increased recombination, either bimolecular or trap-assisted.[117] Fig. 4(e) shows that the binary device exhibits the smallest photo-CELIV peak, indicating higher recombination compared to the ternary systems. Charge carrier mobility values extracted from the intensity-dependent photo-CELIV transients using the simplest analytical formula, reveal no systematic difference in mobility between the various active layer blends, given measurement uncertainty and typical sample-to-sample variations as shown in the SI, Fig. S6.[118] To further clarify the mechanism responsible for the improved photovoltaic performance observed with the incorporation of $PC_{61}BM$ and PCBC6 into the binary system, we conducted device simulations utilizing Setfos (see the ''Device Simulations Part B (steady-state and transient)'' section in the SI). SI Fig. S8(a) illustrates that the experimental *J–V* characteristics are qualitatively replicated by either reducing or entirely disabling Shockley–Read–Hall (SRH) recombination lifetimes when moving from the binary (orange curve) to the ternary PCBC6/$PC_{61}BM$ systems (pink curve). Alternatively, the variations in FF and V_{oc} can also be modelled by increasing hole mobility by a factor of five compared to the binary reference (dashed green line, SI Fig. S8(a)). To differentiate between these two plausible explanations for the observed enhancements in FF and V_{oc} following the addition of a ternary component, we analyzed simulated photo-CELIV transients (SI, Fig. S8(b)). An increase in hole mobility is expected to result in a narrower photo-CELIV peak occurring at an earlier peak time. Conversely, a reduction in SRH recombination primarily leads to an increased peak area, with minimal alterations to peak shape or timing in relation to the binary case. The experimentally measured photo-CELIV transients (Fig. 4(e)) indicate a clear increase in peak area, without significant shifts in peak shape or timing. Therefore, transient CELIV simulations provide strong support for the conclusion that the improvements in FF and V_{oc} observed with the addition of $PC_{61}BM$ or PCBC6 are primarily due to reduced SRH recombination. This interpretation is further corroborated by simulations and experimental results of V_{oc} *versus* illumination intensity (SI, Fig. S8(c) and Fig. 3(f)).

Long-term photo- and thermal stability

Besides the performance of the OSCs, long-term photo and thermal stability of the devices are of paramount importance to ensure their long lifetime operation under stress conditions. To compare the intrinsic stability of the optimized ternary and binary devices, we performed a comparative study by subjecting cells for each variation to photo and thermal stress over a relatively long period. The stability tests were carried out using the following ISOS protocols (Table 4), which revealed the inherent stability of the active layers.

The photo stability tests were conducted following the ISOS-L1-I degradation protocol, while the *J–V* characteristics of the cells were tracked under maximum-power-point-tracking (MPPT) conditions. Fig. 5 depicts the evolution of the photovoltaic figure of merits in normalized scale for each BHJ blend. In particular, binary devices experienced more pronounced reduction in performance with faster decay times compared to the ternary cells. More specifically, the binary

Table 4 Summary of conditions of the thermal/photo ISOS protocols applied in this study

Stability	Light source	Intensity	Atmosphere	Temperature	Encapsulation	MPPT
Photo (ISOS-L1-I)	LED	Equivalent 1 Sun	Nitrogen	RT	No	Yes
Thermal (ISOS-D2-I)	Dark	—	Nitrogen	85 °C	No	—

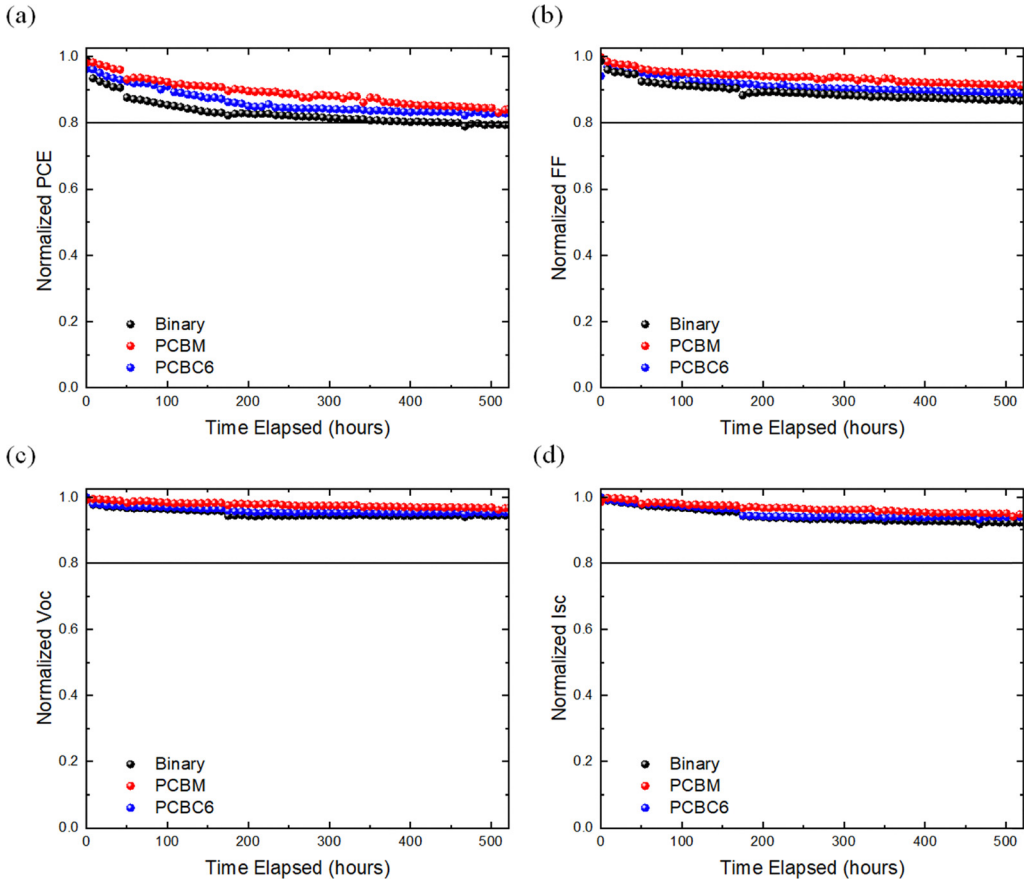

Fig. 5 ISOS-L1I photo stability, normalized (a) PCE, (b) FF, (c) V_{oc}, and (d) I_{sc} of the binary and ternary OSCs.

cells demonstrated a T_{80} lifetime of ~400 hours while after 525 hours of continuous operation at MPPT, they retained ~ 78% of the initial PCE, suffering from V_{oc} and FF losses, attributed to the degradation of both BHJ and hence the interface.[119,120] In contrast, ternary PCBC6 and $PC_{61}BM$-based devices displayed enhanced operational stability, characterized by notably lower degradation rates, sustaining up to ~ 82% and 85% of the initial PCE throughout the same exposure interval. It can be concluded that the slower degradation rate in FF and V_{oc} of the ternary cells is attributed to the incorporation of fullerene molecules which leads to a more stable D/A morphology of the photo-active layers compared to their binary counterparts. Our photo-stability results, considering unencapsulated devices, are among the most photo-stable ternary OSCs in the literature (see Table S3, SI section) and together with the simplicity of accessing or modifying fullerene derivatives this makes our work very attractive as a universal solution for efficient and stable OSCs.

To clarify and to elucidate the underlying factors contributing to the enhanced stability of the ternary-based BHJ cells, we conducted *in situ* Raman spectroscopy and Ultraviolet-Visible (UV-Vis) absorbance measurements. Raman spectroscopy was employed to investigate the photodegradation behaviour of PM6:L8-BO and a representative fullerene ternary blend fullerene-doped blend film. The corresponding Raman spectra of pristine L8-BO, PM6:L8-BO, and PM6:L8-BO:PCBC6 films are shown in the SI, Fig. S9(a). All samples exhibited similar spectral features, dominated by vibrational modes in the 1400–1575 cm^{-1} region. The spectra are primarily governed by PM6-related modes, which are more Raman-active than those of L8-BO. The peak at 1427 cm^{-1} corresponds to collective C–C and C=C stretching vibrations along the thiophene backbone. The band at 1472 cm^{-1} is due to the collective stretching vibrations of C–C and C=C across the backbone thiophenes; 1472 cm^{-1} is predominantly symmetric C=C stretches of thiophenes in benzodithiophene (BDT), neighbouring thiophene to BDT and sidechain thiophenes; 1539 cm^{-1} is stretching in BDT and thienyl benzodithiophene (BDD).[121–123] An example of the photo-induced structural degradation is provided in the SI Fig. S9(b), which shows the evolution of the Raman spectra of a neat PM6:L8-BO film under continuous white light illumination. A progressive decrease in peak intensity is observed, particularly for modes below 1500 cm^{-1}, which decay more rapidly than the 1539 cm^{-1} band and the L8-BO-associated peak at 1556 cm^{-1}. This selective attenuation indicates that PM6 undergoes faster photodegradation than L8-BO under these conditions. These observations align with the recent findings, attributing Raman spectral changes in illuminated PM6:Y6 blends to torsional disorder between the BDT and BDD units in the donor backbone.[123] This previous

work identified PM6 as the primary source of degradation in ambient environments, supporting the broader view that donor polymers constitute a major limitation to blend photostability. Sidechain thiophenes attached to the BDT unit were further implicated in the observed Raman signal reduction, attributed to twisting.[121,124] Recent computational studies of stability concluded that sidechain lesions force the backbone and sidechain twisting observed here, and noted that in ambient environments, oxygen and moisture accelerate this process.[121] To compare the degradation between the blends, kinetics of the main PM6 Raman peaks are presented: 1472 cm^{-1} (greatest decay region at the BDT), and 1427 cm^{-1} and 1539 cm^{-1} as shown in the SI, Fig. S9(c)–(e). Adding PCBC6 to the blend clearly slowed the main degradation pathway in the donor PM6 stabilising the films, consistent with the device stability tests.

Simultaneously, the absorbance profiles of the various blend samples were obtained, pre-and post-light irradiation during our Raman experiments, SI Fig. S10. Among the systems studied, the binary blend exhibits the most rapid degradation, whereas the incorporation of fullerenes leads to a marked suppression of photobleaching, indicating enhanced photostability in the ternary blends. Interestingly, while the absorbance measurements clearly captured the degradation of L8-BO, this is not apparent in the Raman spectra. This discrepancy likely arises from the distinct nature of the two techniques. UV-Vis absorbance spectroscopy probes changes in the electronic transitions, while Raman scattering is sensitive to molecular vibrations. Also, prior works have noted that structural perturbations such as polymer backbone twisting do not necessarily impact the materials' electronic absorption.[121] However, previous works noted significant photoinduced absorbance losses in both PM6 and Y6, consistent with the degradation observed in our study.[123] Furthermore, the impact of fullerenes on the degradation of individual components is notable. In the binary BHJ blend, L8-BO undergoes more rapid photodegradation than PM6. However, this trend is reversed in the ternary blends, where L8-BO demonstrated a slower decay relative to PM6. This inversion suggests that the fullerene derivatives could substantially influence the stability of the NFA, potentially by altering the charge recombination pathways. The observed stabilization of PM6 may arise from a combination of morphological effects and modified photophysical dynamics in the ternary blends.

Furthermore, to evaluate the influence of heat as an accelerating factor on the operational stability of the different cells, thermal stability measurements were performed at 85 °C (ISOS-D2-I). Thermal degradation in the dark occurs in OSCs at elevated temperatures due to structural and morphological instabilities of the absorber materials. In particular, the ISOS-D2-I tests (Fig. 6) for the binary cells demonstrated severe degradation with a T_{80} lifetime of ~4 hours, while retaining 33% of their initial PCE after being under continuous thermal stress for ~100 hours (average value from N = 5 individual cells). On the other hand, the ternary cells showed superior thermal stability compared to the binary counterparts with a T_{80} lifetime between ~12 to 16 hours, retaining ~58% and ~60% of their initial PCE after 100 hours for PCBC6 and $PC_{61}BM$, respectively (average value from N = 6 individual cells). The enhanced thermal stability of the ternary BHJ systems signifies an increased resilience to morphology-related degradation of the ternary photo-active layers in the presence of extreme heat stress conditions. It is worth noting that the increased thermal stability of the ternary devices was mainly attributed to the resilient FF and V_{oc} of the degraded devices. In general, the beneficial role of morphological modification, including π–π stacking and lamellar stacking, and its correlation with stability (photo and thermal stability) has been recently reported in the literature of OSCs with ternary components, other than fullerenes.[19,125] This further supports the validity of our findings and the relevant discussion.

To elucidate the role of fullerene molecules in modulating the thermal stability of organic blends, detailed atomistic simulations were conducted using full atomic resolution classical molecular dynamics (MD) simulations. Three systems, reflecting experimental compositions, were modelled, respectively. Comprehensive simulation protocols and model parameters are provided in the ''Model system's setup'' SI section. MD simulations revealed the tendency of PM6 and L8-BO to cluster thereby forming agglomerates of similar and dissimilar molecules held together *via* weak non-covalent interactions including delocalized π–π stacking among PM6 monomers (Movie S1), between PM6 and L8-BO molecules (Movie S3), and dispersion forces between carbon backbone and side chains of L8-BO molecules (Movie S2) as visually validated with the help of NCIPLOT (see the SI for details). These interactions, albeit weak, are apparently strong enough to induce microphase segregation manifested by the formation of local PM6- and L8-BO-rich domains. This association in domains, and the associated imparted inhomogeneity and anisotropy were captured clearly by the large discrepancy in the mass and number density profiles for the binary blend shown in Fig. 6(e) and (f). It is evident that the $PC_{61}BM$-ternary blend, was the most uniformly distributed and most homogeneous of the three, directly followed by the PCBC6-ternary blend. Last, the binary system appeared to be the most inhomogeneous due to the profound clustering of its components. The findings evinced by the heat maps of Fig. 6(e) and (f) were further corroborated by computing each system's gyration tensor S, with the help of which shape descriptors such as the asphericity b and the relative shape anisotropy k could be computed. The reader is referred to the SI for a detailed description of these quantities. Briefly, the smaller b and k are, the more symmetric and thus more uniform and homogeneous a system is. It appears that the $PC_{61}BM$-ternary blend exhibits the smallest values of b and k, followed by the PCBC6-ternary blend, with the binary system yielding substantially larger b and k values (see Table S6). Taken together, these findings indicate that the presence of fullerenes within the system suppresses the formation of local agglomerates of PM6, L8-BO and combinations thereof leading to a more homogeneous distribution of components. Nonetheless, it was not clear why $PC_{61}BM$ performs better in that regard than PCBC6. One possible reason could be associated with the shorter side chain of $PC_{61}BM$ which would potentially allow

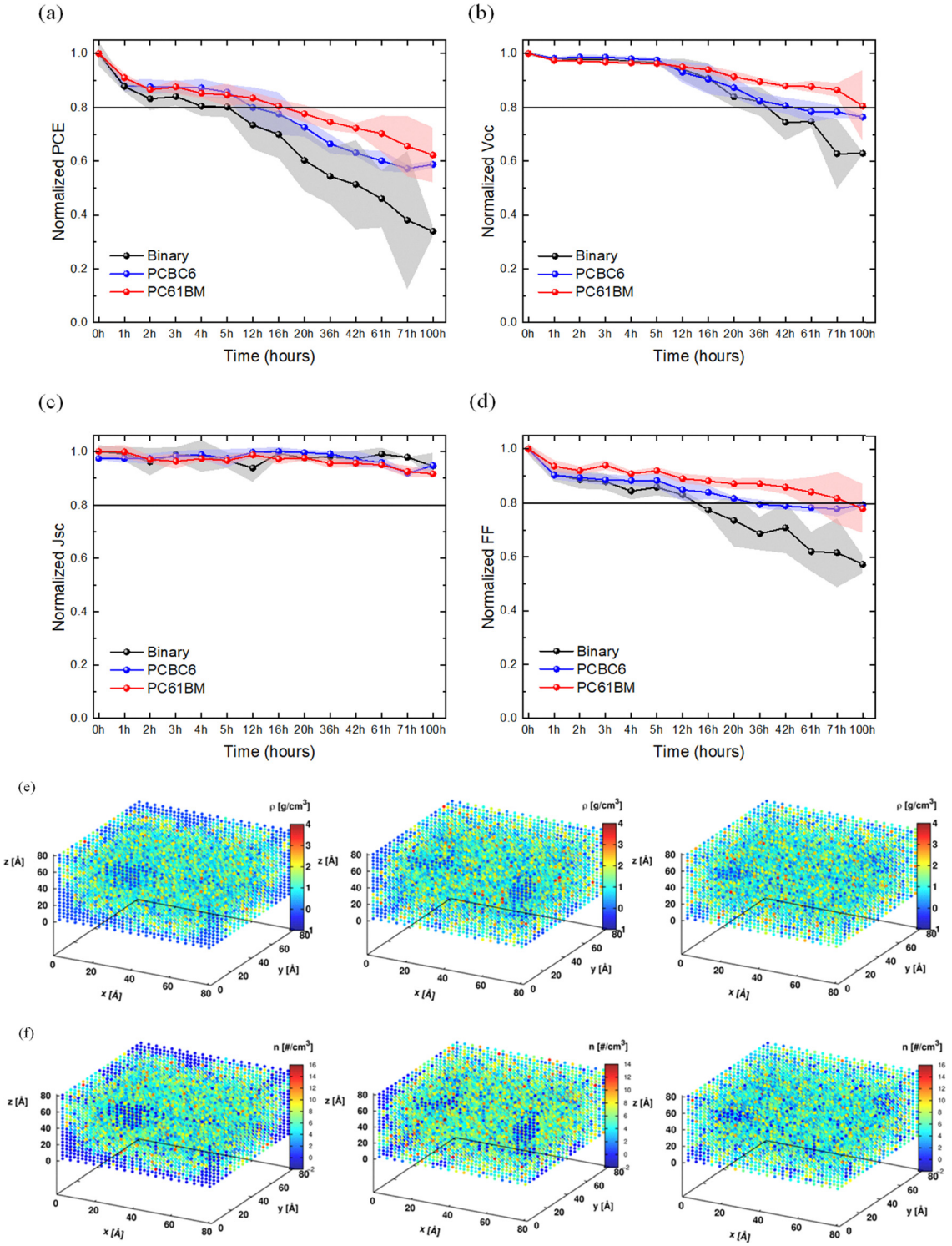

Fig. 6 ISOS-D2-I thermal stability (85 °C inert atmosphere), normalized (a) PCE, (b) V_{oc}, (c) J_{sc} and (d) FF graphs. Solid lines correspond to the average values of N = 5 individual cells for each blend, and the coloured area shows the deviation in each variation. (e) Heat maps of the mass and (f) number density of all system: left column (system 1), middle column (system 2) and right column (system 3).

for higher molecular mobility and diffusivity. The lengthier side chain of PCBC6 could have been responsible for the formation of local entanglement with neighbouring molecules hampering its mobility and thus its ability to prevent agglomeration of PM6 and L8-BO molecules. To validate this hypothesis, the self-diffusion coefficient D of the centre of mass of $PC_{61}BM$ and PCBC6 molecules was computed in their corresponding systems (SI, Fig. S11). As originally hypothesized, the diffusivity D of $PC_{61}BM$ was 1.47×10^{-11} m^2 s^{-1}, about 27% larger than its PCBC6 counterpart. Increased

diffusivity explains, at least partially, why $PC_{61}BM$ homogenizes the mixture faster and more efficiently than PCBC6. At this point, a clarification is required. Improved component dispersion within a system is of paramount importance as it ensures homogeneity and isotropic behaviour. It is worth noting that because of the large discrepancy in the thermal expansion coefficients α_v of pure PM6 and pure L8-BO, computed to be 5.32×10^{-4} K^{-1} and 2.99×10^{-5} K^{-1} (almost 20× smaller), respectively (SI, Fig. S12), the formation of PM6- and L8-BO-rich domains is detrimental as it leads to a largely anisotropic and non-uniform thermal response of the system. This substantial disparity in the thermal response can, in turn, generate enormous interfacial stresses which can exceed 150 MPa, enough to deform copper or induce material delamination.[126] Therefore, it is crucial for improved stability and material longevity to ensure good component dispersion within the system. The addition of PCBC6 or $PC_{61}BM$ into the binary system ensures better component dispersion, which, in turn, translates into smaller thermal expansion mismatch resulting in values of 2.87×10^{-4} K^{-1} and 3.37×10^{-4} K^{-1} for $PC_{61}BM$ and PCBC6 systems, respectively (SI, Fig. S12). Taken all together, $PC_{61}BM$ functions as a morphology regulator ensuring better dispersion of components, more uniform and isotropic thermal and mechanical behaviour across the system and thus improved thermal stability, in line with the experimental results presented in Fig. 6.

Upscaling potential

In addition to efficiency and stability, another important metric that needs to be discussed and optimized towards the industrialization of OSCs is their upscaling potential. For the purpose of investigating the scaling potential of the ternary cells, we expanded the active device area from the 0.09 cm^2 (small cells) to 3.8 cm^2 (mini-modules size). The mini modules consisted of 4 individual sub-cells (active area of 0.95 cm^2 each) connected monolithically in series as illustrated in Fig. 7(c). In particular, the champion PM6:L8-BO-based mini modules demonstrated a maximum PCE of 12.90% with a J_{sc} value of 6.46 mA cm^{-2}, a V_{oc} of 3.34 V, and a FF of 59% (Fig. 7(a)). The PM6:L8-BO:$PC_{61}BM$ and PM6:L8-BO:PCBC6-based mini modules on the other hand showed a maximum PCE of 13.32% with a J_{sc} of 6.53 mA cm^{-2}, a V_{oc} of 3.40 V, and a FF of 60% and PCE of 13.70% with a J_{sc} of 6.47 mA cm^{-2}, a FF of 62% and a V_{oc} of 3.41 V, respectively (Fig. 7(a)). Notably, the mini-modules demonstrated consistent performance trends similar to the small-area cells, with main improvements in FF and V_{oc} and marginal differences in J_{sc}, respectively. As a result, the ternary-based mini modules demonstrated enhanced power output values compared to the

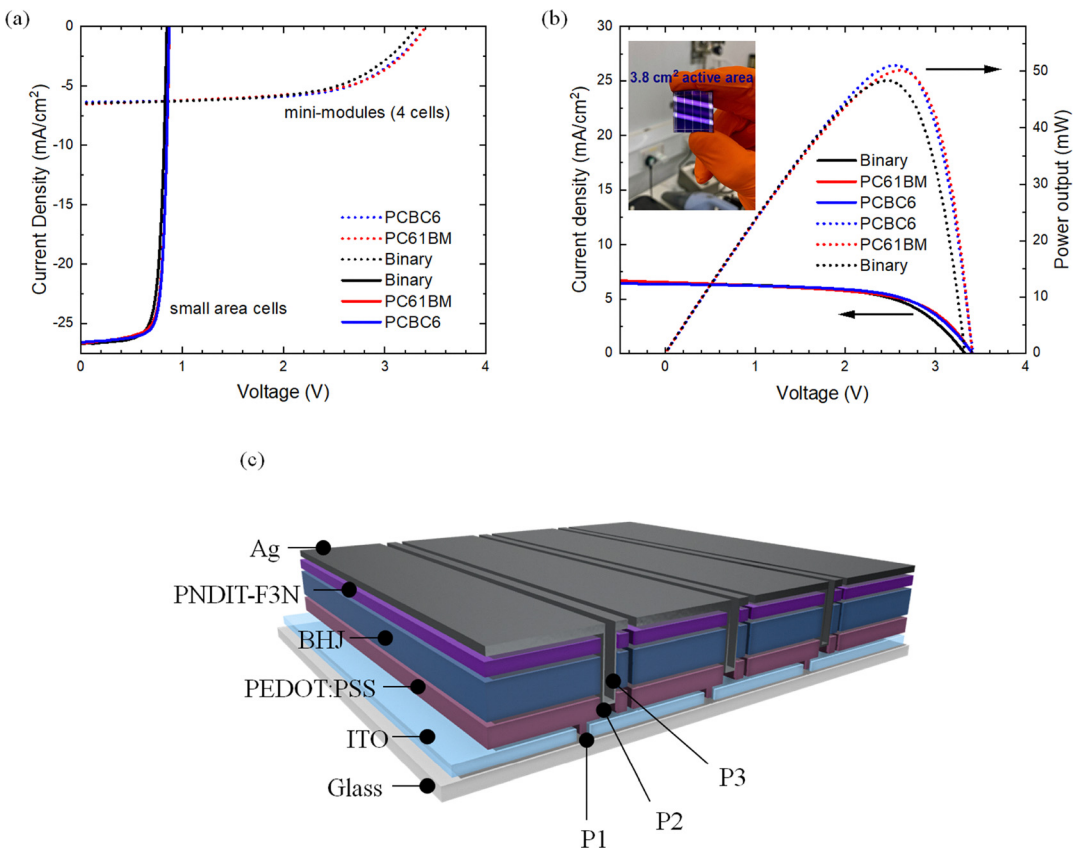

Fig. 7 (a) *J–V* characteristics of mini modules (4 cells layout) and small area cells for binary ternary BHJ systems, (b) power output and current density–voltage curves for binary and ternary-based BHJ mini modules, and (c) schematic illustration of the solar mini modules (cross-sectional view).

binary mini modules exhibiting 50 mW and 51 mW for $PC_{61}BM$ and PCBC6-based ternary compared to 48 mW, respectively. The aforementioned results highlighted the upscaling potential of this strategy highlighting the beneficial role of the fullerene derivatives not only for improving the morphology of small area cells but also in homogenizing the active layer morphology even on larger area mini-modules.

Conclusions

In summary, our findings demonstrate an effective ternary strategy for enhancing the efficiency, stability and up-scalability of PM6:L8-BO BHJ-based OSCs *via* the incorporation of fullerene derivatives such as $PC_{61}BM$ and PCBC6. Notably, fullerene derivatives lead to enhanced OSC FF and V_{oc} values by suppressing the trap-assistant recombination, as evidenced by the reduced non-radiative voltage losses, and improving charge transport and collection within the device, relevant to favourable energy level alignment. The small addition of fullerene derivatives has a minor effect on the energy level alignment; however, the drastic modification of the blend morphology provides the necessary conditions for reduced non-radiative recombination processes. This implies that the dominant mechanism for the increased V_{oc} is related to the suppressed non-radiative recombination for the ternary blends. In particular, ternary cells demonstrated efficient charge collection, attributed to the improved blend morphology and molecular packing as corroborated by AFM and GIWAXS measurements. Moreover, electrochemical and transient analysis further confirm increased built-in potential and prolonged carrier lifetime in the ternary devices. Stability protocols in conjunction with *in situ* spectroscopies and molecular dynamics simulations revealed that the fullerene molecules affect the degradation pathway of the photo-active layers, while simultaneously acting as morphology regulators promoting uniform dispersion and mitigating thermal expansion mismatches. As a result, ternary $PC_{61}BM$ and PCBC6-based cells demonstrate enhanced long-term photo- and thermal stability. Scalable devices (mini-modules) with an active area of 3.8 cm^2 demonstrated similar composition-dependent performance trends compared to small-area cells, underscoring the suitability of this approach for scalable production of OSCs. Overall, this study highlights fullerene derivatives as significant multifunctional additives for next-generation NFA-ternary OSCs, suggesting a promising strategy to achieve high performance, stable and large area photovoltaics.

Author contributions

A. P. and D. K. conceived the idea. A. P., D. K., G. K and S. R. P. S discussed, planned the content, analysed the literature. A. P. designed, fabricated and characterized the devices. K. A. performed the EIS and *C–V* measurements and analyzed the data. E. Y-H. H. carried out the GIWAXS characterization and analysis. N. L. performed the MD simulations. W. X. conducted the EQE_{EL} measurement and data analysis under the supervision of S. D. S. G. P. performed the *C–V* simulations models. S. J carried out the Photo-CELIV and transient simulation models. L. A. and S. D. conducted the *in situ* RAMAN and UV-Vis characterization. E. R. assisted with the AFM measurements. A. P, G. K. and N. L contributed to the relevant data analysis and the revision of the first draft. A. P., G. K., G. P., N. L., D. K. and S. R. P. S., contributed to the preparation of the manuscript. S. R. P. S. supervised the project. All authors contributed to manuscript preparation, revision and approved its submission for publication.

Conflicts of interest

S. D. S. is a co-founder of Swift Solar, Inc.

Data availability

The data supporting this article have been included as part of the supplementary information (SI). Supplementary information is available. See DOI: https://doi.org/10.1039/d5mh02065d.

Acknowledgements

A. P. acknowledges the funding from UKRI (iCase/UKRI) for his studentship, grant number EP/T517616. A. P and S. R. P. S gratefully acknowledge the support from QinetiQ and MUSICODE H2020. A. P., D. K., and S. R. P. S. deeply appreciate the research collaboration with Nano-C Inc. for kindly providing all the fullerene derivative molecules used in this case study. N. L. gratefully acknowledges computational time granted from the National Infrastructures for Research and Technology S. A. (GRNET) in the National HPC facility – ARIS – under project ID pr018007. G. P. gratefully acknowledges the Hellenic Foundation for Research and Innovation (HFRI) under ''Sub-action 2 for Funding Projects in Leading-Edge Sectors – RRFQ: Basic Research Financing (Horizontal support for all Sciences)'', MultiCool (15117). B. M. G. received funding from the European Union's Framework programme for Research and Innovation HORIZON EUROPE (2021–2027) under the Marie Skłodowska-Curie Action Postdoctoral Fellowships (European Fellowship) 101153827. E. Y.-H. H. acknowledges Xaar plc for her PhD studentship. W. X and S. D. S. acknowledge the funding from EPSRC, EP/V027131/1.

References

1 B. Kan, Q. Zhang, M. Li, X. Wan, W. Ni, G. Long, Y. Wang, X. Yang, H. Feng and Y. Chen, *J. Am. Chem. Soc.*, 2014, **136**, 20.
2 D. Corzo, K. Almasabi, E. Bihar, S. Macphee, D. Rosas-Villalva, N. Gasparini, S. Inal and D. Baran, *Adv. Mater. Technol.*, 2019, **4**, 1900040.
3 A. Liang, Y. Sun, S. Chung, J. Shin, K. Sun, C. Zhu, J. Zhao, Z. Zhao, Y. Zhong, G. Zhang, K. Cho and Z. Kan, *Nanomicro Lett.*, 2025, **17**, 72.

4 J. Han, F. Bao, D. Huang, X. Wang, C. Yang, R. Yang, X. Jian, J. Wang, X. Bao and J. Chu, *Adv. Funct. Mater.*, 2020, **30**, 2003654.
5 C. Liu, C. Xiao, C. Xie and W. Li, *Nano Energy*, 2021, **89**, 106399.
6 K. Fukuda, K. Yu and T. Someya, *Adv. Energy Mater.*, 2020, **10**, 2000765.
7 L. Xie, Z. Chen, D. Yang, X. Yu, X. Tong, J. Ge, W. Song, S. Yang, J. Zhu, P. Ding, G. Lu, X. Li, M. Long, J. Li, B. Zou, T. Liu, Q. Liu and Z. Ge, *Energy Environ. Sci.*, 2024, **17**, 7838–7849.
8 W. Song, Q. Ye, Z. Chen, J. Ge, L. Xie and Z. Ge, *Adv. Mater.*, 2024, **36**, 2311170.
9 Z. Wang, X. Wang, L. Tu, H. Wang, M. Du, T. Dai, Q. Guo, Y. Shi and E. Zhou, *Angew. Chem., Int. Ed.*, 2024, **63**, e202319755.
10 A. Panagiotopoulos, T. Maksudov, G. Kakavelakis, G. Perrakis, E. A. Alharbi, D. Kutsarov, F. H. Isikgor, S. Alfihed, K. Petridis, M. Kafesaki, S. R. P. Silva, T. D. Anthopoulos and M. Graetzel, *Appl. Phys. Rev.*, 2023, **10**, 41303.
11 D. I. Kutsarov, E. New, F. Bausi, A. Zoladek-Lemanczyk, F. A. Castro and S. R. P. Silva, *Sol. Energy Mater. Sol. Cells*, 2017, **161**, 388–396.
12 S. V. Subramaniam, D. Kutsarov, T. Sauermann and S. B. Meier, *Energy Technol.*, 2020, **8**, 2000234.
13 K. D. G. I. Jayawardena, L. J. Rozanski, C. A. Mills, M. J. Beliatis, N. A. Nismy and S. R. P. Silva, *Nanoscale*, 2013, **5**, 8411–8427.
14 C. T. G. Smith, R. W. Rhodes, M. J. Beliatis, K. D. G. Imalka Jayawardena, L. J. Rozanski, C. A. Mills and S. R. P. Silva, *Appl. Phys. Lett.*, 2014, **105**, 73304.
15 K. D. G. I. Jayawardena, R. Rhodes, K. K. Gandhi, M. R. R. Prabhath, G. D. M. R. Dabera, M. J. Beliatis, L. J. Rozanski, S. J. Henley and S. R. P. Silva, *J. Mater. Chem. A*, 2013, **1**, 9922–9927.
16 C. Li, Y. Cai, P. Hu, T. Liu, L. Zhu, R. Zeng, F. Han, M. Zhang, M. Zhang, J. Lv, Y. Ma, D. Han, Q. Lin, J. Xu, N. Yu, J. Qiao, J. Wang, X. Zhang, J. Xia, Z. Tang, L. Ye, X. Li, Z. Xu, X. Hao, Q. Peng, F. Liu, L. Guo and H. Huang, *Nat. Mater.*, 2025, **24**, 1626–1634.
17 J. Dong, Y. Li, C. Liao, X. Xu, L. Yu, R. Li and Q. Peng, *Energy Environ. Sci.*, 2025, **18**, 4982–4995.
18 C. Chen, L. Wang, W. Xia, K. Qiu, C. Guo, Z. Gan, J. Zhou, Y. Sun, D. Liu, W. Li and T. Wang, *Nat. Commun.*, 2024, **15**(1), 6865.
19 Z. Ling, J. Wu, J. P. Jurado, C. E. Petoukhoff, S. Y. Jeong, D. Naphade, M. Babics, X. Chang, H. Faber, S. Doukas, E. Lidorikis, M. I. Nugraha, M. He, M. Alqurashi, Y. Lin, X. Sun, H. Hu, H. Y. Woo, S. De Wolf, L. Tsetseris, F. Laquai, D. Yu, E. Wang and T. D. Anthopoulos, *Mater. Sci. Eng., R*, 2025, **163**, 100922.
20 H. Chen, S. Y. Jeong, J. Tian, Y. Zhang, D. R. Naphade, M. Alsufyani, W. Zhang, S. Griggs, H. Hu, S. Barlow, H. Y. Woo, S. R. Marder, T. D. Anthopoulos, I. McCulloch and Y. Lin, *Energy Environ. Sci.*, 2023, **16**, 1062–1070.
21 J. Hou, O. Inganas, R. H. Friend and F. Gao, Nature Publishing Group, 2018, preprint, DOI: 10.1038/NMAT5063.
22 H. Xu, J. Han, M. Babics, L. Huerta Hernandez, D. Rosas Villalva, M. Sanviti, J. Bertrandie, Y. Zhang, Y. Liu, H. Chen, L. Zhao, J. Troughton, J. Martin, F. Laquai, S. De Wolf and D. Baran, *Nat. Photonics*, 2025, **19**, 415–425.
23 L. Zhan, S. Yin, Y. Li, S. Li, T. Chen, R. Sun, J. Min, G. Zhou, H. Zhu, Y. Chen, J. Fang, C. Q. Ma, X. Xia, X. Lu, H. Qiu, W. Fu and H. Chen, *Adv. Mater.*, 2022, **34**, 2206269.
24 L. Zhu, M. Zhang, J. Xu, C. Li, J. Yan, G. Zhou, W. Zhong, T. Hao, J. Song, X. Xue, Z. Zhou, R. Zeng, H. Zhu, C. C. Chen, R. C. I. MacKenzie, Y. Zou, J. Nelson, Y. Zhang, Y. Sun and F. Liu, *Nat. Mater.*, 2022, **21**, 656–663.
25 Y. Wang, J. Yu, R. Zhang, J. Yuan, S. Hultmark, C. E. Johnson, N. P. Gallop, B. Siegmund, D. Qian, H. Zhang, Y. Zou, M. Kemerink, A. A. Bakulin, C. Müller, K. Vandewal, X. K. Chen and F. Gao, *Nat. Energy*, 2023, **8**, 978–988.
26 P. Bi, S. Zhang, Z. Chen, Y. Xu, Y. Cui, T. Zhang, J. Ren, J. Qin, L. Hong, X. Hao and J. Hou, *Joule*, 2021, **5**, 2408–2419.
27 C. Wöpke, C. Göhler, M. Saladina, X. Du, L. Nian, C. Greve, C. Zhu, K. M. Yallum, Y. J. Hofstetter, D. Becker-Koch, N. Li, T. Heumüller, I. Milekhin, D. R. T. Zahn, C. J. Brabec, N. Banerji, Y. Vaynzof, E. M. Herzig, R. C. I. MacKenzie and C. Deibel, *Nat. Commun.*, 2022, **13**, 1–8.
28 S. Zeiske, O. J. Sandberg, N. Zarrabi, W. Li, P. Meredith and A. Armin, *Nat. Commun.*, 2021, **12**, 1–7.
29 A. Foertig, J. Kniepert, M. Gluecker, T. Brenner, V. Dyakonov, D. Neher and C. Deibel, *Adv. Funct. Mater.*, 2014, **24**, 1306–1311.
30 L. Duan and A. Uddin, *Adv. Sci.*, 2020, **7**, 1903259.
31 X. Duan, W. Song, J. Qiao, X. Li, Y. Cai, H. Wu, J. Zhang, X. Hao, Z. Tang, Z. Ge, F. Huang and Y. Sun, *Energy Environ. Sci.*, 2022, **15**, 1563–1572.
32 X. Zhu, K. Wang, J. He, L. Zhang, H. Yu, D. He and B. Hu, *J. Phys. Chem. C*, 2019, **123**, 20691–20697.
33 Q. Liang, W. Li, H. Lu, Z. Yu, X. Zhang, Q. Dong, C. Song, Z. Miao and J. Liu, *ACS Appl. Energy Mater.*, 2023, **6**, 31–50.
34 H. Tian, Y. Ni, W. Zhang, Y. Xu, B. Zheng, S. Y. Jeong, S. Wu, Z. Ma, X. Du, X. Hao, H. Y. Woo, L. Huo, X. Ma and F. Zhang, *Energy Environ. Sci.*, 2024, **17**, 5173–5182.
35 X. He, L. Yin and Y. Li, *J. Mater. Chem. C*, 2019, **7**, 2487–2521.
36 H. Zhou, Y. Sun, M. Zhang, Y. Ni, F. Zhang, S. Young Jeong, T. Huang, X. Li, H. Y. Woo, J. Zhang, W. Y. Wong, X. Ma and F. Zhang, *Sci. Bull.*, 2024, **69**, 2862–2869.
37 S. Liu, J. Yuan, W. Deng, M. Luo, Y. Xie, Q. Liang, Y. Zou, Z. He, H. Wu and Y. Cao, *Nat. Photonics*, 2020, **14**, 300–305.
38 D. He, F. Zhao, C. Wang, Y. Lin, D. He, F. Zhao, C. Wang and Y. Lin, *Adv. Funct. Mater.*, 2022, **32**, 2111855.
39 J. Zhang, H. S. Tan, X. Guo, A. Facchetti and H. Yan, *Nat. Energy*, 2018, **3**, 720–731.
40 X. Liu, Y. Yan, Y. Yao, Z. Liang, X. Liu, Y. Yan, Z. Liang and Y. Yao, *Adv. Funct. Mater.*, 2018, **28**, 1802004.

41 Z. Zhao, J. Zhao, S. Chung, K. Cho, W. Xu and Z. Kan, *ACS Mater. Lett.*, 2023, **5**, 1718–1726.
42 C. Zhu, S. Chung, J. Zhao, Y. Sun, B. Zhao, Z. Zhao, S. Kim, K. Cho and Z. Kan, *Adv. Sci.*, 2023, **10**, 2303150.
43 T. Huang, Y. Zhang, J. Wang, Z. Cao, S. Geng, H. Guan, D. Wang, Z. Zhang, Q. Liao and J. Zhang, *Nano Energy*, 2024, **121**, 109226.
44 X. Li, A. Tang, H. Wang, Z. Wang, M. Du, Q. Guo, Q. Guo and E. Zhou, *Angew. Chem., Int. Ed.*, 2023, **62**, e202306847.
45 Z. Liu, M. Zhang, L. Zhang, S. Y. Jeong, S. Geng, H. Y. Woo, J. Zhang, F. Zhang and X. Ma, *Chem. Eng. J.*, 2023, **471**, 144711.
46 J. Lee, S.-J. Ko, M. Seifrid, H. Lee, C. McDowell, B. R. Luginbuhl, A. Karki, K. Cho, T.-Q. Nguyen, G. C. Bazan, J. Lee, S. Ko, M. Seifrid, C. McDowell, B. R. Luginbuhl, A. Karki, T. Nguyen, G. C. Bazan, H. Lee and K. Cho, *Adv. Energy Mater.*, 2018, **8**, 1801209.
47 L. Zhan, S. Li, H. Zhang, F. Gao, T.-K. Lau, X. Lu, D. Sun, P. Wang, M. Shi, C.-Z. Li, H. Chen, L. Zhan, S. Li, M. Shi, C. Li, H. Chen, H. Zhang, F. Gao, T. Lau, X. Lu, D. Sun and P. Wang, *Adv. Sci.*, 2018, **5**, 1800755.
48 W. Wu, G. Zhang, X. Xu, S. Wang, Y. Li, Q. Peng, W. Wu, G. Zhang, X. Xu, S. Wang, Y. Li and Q. Peng, *Adv. Funct. Mater.*, 2018, **28**, 1707493.
49 T. Huang, Z. Zhang, Q. Liao, D. Wang, Y. Zhang, S. Geng, H. Guan, Z. Cao, Y. Huang and J. Zhang, *Small*, 2023, **19**, 2303399.
50 T. Chen, S. Li, Y. Li, Z. Chen, H. Wu, Y. Lin, Y. Gao, M. Wang, G. Ding, J. Min, Z. Ma, H. Zhu, L. Zuo and H. Chen, *Adv. Mater.*, 2023, **35**, 2300400.
51 R. Sun, T. Wang, Q. Fan, M. Wu, X. Yang, X. Wu, Y. Yu, X. Xia, F. Cui, J. Wan, X. Lu, X. Hao, A. K. Y. Jen, E. Spiecker and J. Min, *Joule*, 2023, **7**, 221–237.
52 M. Zhang, Z. Xiao, W. Gao, Q. Liu, K. Jin, W. Wang, Y. Mi, Q. An, X. Ma, X. Liu, C. Yang, L. Ding, F. Zhang, M. Zhang, W. Wang, Q. An, X. Ma, F. Zhang, Z. Xiao, Q. Liu, K. Jin, Y. Mi, X. Liu, L. Ding, W. Gao and C. Yang, *Adv. Energy Mater.*, 2018, **8**, 1801968.
53 K. Jiang, G. Zhang, G. Yang, J. Zhang, Z. Li, T. Ma, H. Hu, W. Ma, H. Ade, H. Yan, K. Jiang, G. Zhang, J. Zhang, H. Yan, G. Yang, Z. Li, T. Ma, H. Hu, W. Ma and H. Ade, *Adv. Energy Mater.*, 2018, **8**, 1701370.
54 T. Y. Huang, D. Patra, Y. S. Hsiao, S. H. Chang, C. G. Wu, K. C. Ho and C. W. Chu, *J. Mater. Chem. A*, 2015, **3**, 10512–10518.
55 D. Angmo, M. Bjerring, N. C. Nielsen, B. C. Thompson and F. C. Krebs, *J. Mater. Chem. C*, 2015, **3**, 5541–5548.
56 M. Zhang, W. Gao, F. Zhang, Y. Mi, W. Wang, Q. An, J. Wang, X. Ma, J. Miao, Z. Hu, X. Liu, J. Zhang and C. Yang, *Energy Environ. Sci.*, 2018, **11**, 841–849.
57 K. Li, Y. Wu, Y. Tang, M. A. Pan, W. Ma, H. Fu, C. Zhan and J. Yao, *Adv. Energy Mater.*, 2019, **9**, 1901728.
58 K. Li, Y. Wu, X. Li, H. Fu and C. Zhan, *Sci. China: Chem.*, 2020, **63**, 490–496.
59 W. Xu and F. Gao, *Mater. Horiz.*, 2018, **5**, 206–221.
60 N. S. Sariciftci, L. Smilowitz, A. J. Heeger and F. Wudl, *Science*, 1992, **258**, 1474–1476.
61 D. Deng, Y. Zhang, J. Zhang, Z. Wang, L. Zhu, J. Fang, B. Xia, Z. Wang, K. Lu, W. Ma and Z. Wei, *Nat. Commun.*, 2016, **7**, 1–9.
62 J. Zhao, Y. Li, G. Yang, K. Jiang, H. Lin, H. Ade, W. Ma and H. Yan, *Nat. Energy*, 2016, **1**, 1–7.
63 X. Liu, S. Du, Z. Fu, C. Chen, J. Tong, J. Li, N. Zheng, R. Zhang and Y. Xia, *Sol. Energy*, 2021, **222**, 18–26.
64 J. Gao, J. Wang, Q. An, X. Ma, Z. Hu, C. Xu, X. Zhang and F. Zhang, *Sci. China: Chem.*, 2020, **63**, 83–91.
65 Y. Zhou, L. Hu, X. Tang, Z. Wang, L. Jiang, M. Li and R. Qin, *Mater. Lett.*, 2023, **341**, 134291.
66 H. Zhou, C. Liu, S. Liu, Z. Zhang, S. Sun, W. Xu, X. Ma, J. Wang, Y. Xu, X. Du, S. Y. Jeong, H. Y. Woo, F. Zhang and Q. Sun, *Small*, 2024, **20**, 2308216.
67 M. A. Pan, T. K. Lau, Y. Tang, Y. C. Wu, T. Liu, K. Li, M. C. Chen, X. Lu, W. Ma and C. Zhan, *J. Mater. Chem. A*, 2019, **7**, 20713–20722.
68 Y. Yan, X. Zhou, F. Zhang, J. Zhou, T. lin, Y. Zhu, D. Xu, X. Ma, Y. Zou and X. Li, *J. Mater. Chem. A*, 2022, **10**, 23124–23133.
69 T. Ahmad, B. Wilk, E. Radicchi, R. Fuentes Pineda, P. Spinelli, J. Herterich, L. A. Castriotta, S. Dasgupta, E. Mosconi, F. De Angelis, M. Kohlstädt, U. Würfel, A. Di Carlo and K. Wojciechowski, *Adv. Funct. Mater.*, 2020, **30**, 2004357.
70 G. Ashiotis, A. Deschildre, Z. Nawaz, J. P. Wright, D. Karkoulis, F. E. Picca and J. Kieffer, *Appl. Crystallogr.*, 2015, **48**, 510–519.
71 T. G. Dane, The pygix library, https://github.com/tgdane/pygix.
72 D. I. Kutsarov, I. Rašović, A. Zachariadis, A. Laskarakis, M. A. Lebedeva, K. Porfyrakis, C. A. Mills, M. J. Beliatis, B. Fisher, K. Bruchlos, S. Ludwigs, S. Logothetidis and S. R. P. Silva, *Adv. Electron. Mater.*, 2016, **2**, 1600362.
73 J. G. Sánchez, A. Cabrera-Espinoza, E. Martínez-Ferrero, J. L. Delgado and E. Palomares, *Mater. Adv.*, 2022, **3**, 1071–1078.
74 C. B. Nielsen, S. Holliday, H. Y. Chen, S. J. Cryer and I. McCulloch, *Acc. Chem. Res.*, 2015, **48**, 2803–2812.
75 Y. Wu, Y. Li, B. van der Zee, W. Liu, A. Markina, H. Fan, H. Yang, C. Cui, Y. Li, P. W. M. Blom, D. Andrienko and G. J. A. H. Wetzelaer, *Sci. Rep.*, 2023, **13**, 1–8.
76 Y. Ran, C. Liang, Z. Xu, W. Jing, X. Xu, Y. Duan, R. Li, L. Yu, Q. Peng, Y. Ran, C. Liang, Z. Xu, W. Jing, X. Xu, L. Yu, Q. Peng, Y. Duan and R. Li, *Adv. Funct. Mater.*, 2024, **34**, 2311512.
77 C. Li, J. Zhou, J. Song, J. Xu, H. Zhang, X. Zhang, J. Guo, L. Zhu, D. Wei, G. Han, J. Min, Y. Zhang, Z. Xie, Y. Yi, H. Yan, F. Gao, F. Liu and Y. Sun, *Nat. Energy*, 2021, **6**, 605–613.
78 K. Weng, L. Ye, L. Zhu, J. Xu, J. Zhou, X. Feng, G. Lu, S. Tan, F. Liu and Y. Sun, *Nat. Commun.*, 2020, **11**, 1–9.
79 X. Li, Y. Wu, H. Yang, H. Fan, K. Hu, C. Cui and Y. Li, *Adv. Funct. Mater.*, 2025, **35**, 2503986.

80 Y. Xu, C. Liu, W. Zou, N. Qiu, X. Jiang, H. Xu, P. Cai, R. Yang, X. Wang, C. Shen, L. Ni, L. Geng, Y. Kan, Y. Sun and K. Gao, *ACS Mater. Lett.*, 2024, **6**, 1920–1928.
81 K. An, W. Zhong, F. Peng, W. Deng, Y. Shang, H. Quan, H. Qiu, C. Wang, F. Liu, H. Wu, N. Li, F. Huang and L. Ying, *Nat. Commun.*, 2023, **14**, 1–11.
82 M. Zhang, L. Zhu, C. Qiu, T. Hao, Y. Jiang, S. Leng, J. Chen, G. Zhou, Z. Zhou, Y. Zou, X. Su, Z. Shi, H. Zhu, Y. Zhang, T. P. Russell, X. Zhu and F. Liu, *Small Science*, 2022, **2**, 2100092.
83 R. Ding, S. Wang, Z. Yang, J. Weng, C. Li, Z. Liu, Z. Zhang, J. Zhang, Z. Tang, Y. Cai and H. Huang, *J. Mater. Chem. A*, 2025, **13**, 33356–33364.
84 A. Panagiotopoulos, G. Kakavelakis, K. Almpanidis, L. Askew, D. I. Kutsarov and S. R. P. Silva, *J. Mater. Chem. A*, 2025, **13**, 8774–8789.
85 M. C. Scharber, D. Mühlbacher, M. Koppe, P. Denk, C. Waldauf, A. J. Heeger and C. J. Brabec, *Adv. Mater.*, 2006, **18**, 789–794.
86 S. H. Yoo, J. M. Kum and S. O. Cho, *Nanoscale Res. Lett.*, 2011, **6**, 1–7.
87 S. H. Yoo, J. M. Kum, G. Ali, S. H. Heo and S. O. Cho, *Nanoscale Res. Lett.*, 2012, **7**, 1–6.
88 Solarmer, 2022, preprint.
89 G. Kakavelakis, I. Vangelidis, A. Heuer-Jungemann, A. G. Kanaras, E. Lidorikis, E. Stratakis and E. Kymakis, *Adv. Energy Mater.*, 2016, **6**, 1501640.
90 G. Kakavelakis, A. E. Del Rio Castillo, V. Pellegrini, A. Ansaldo, P. Tzourmpakis, R. Brescia, M. Prato, E. Stratakis, E. Kymakis and F. Bonaccorso, *ACS Nano*, 2017, **11**, 3517–3531.
91 C. G. Shuttle, R. Hamilton, B. C. O'Regan, J. Nelson and J. R. Durrant, *Proc. Natl. Acad. Sci. U. S. A.*, 2010, **107**, 16448–16452.
92 V. D. Mihailetchi, L. J. A. Koster, J. C. Hummelen and P. W. M. Blom, *Phys. Rev. Lett.*, 2004, **93**, 216601.
93 J. L. Wu, F. C. Chen, Y. S. Hsiao, F. C. Chien, P. Chen, C. H. Kuo, M. H. Huang and C. S. Hsu, *ACS Nano*, 2011, **5**, 959–967.
94 C. M. Proctor and T. Q. Nguyen, *Appl. Phys. Lett.*, 2015, **106**, 83301.
95 J. Vollbrecht, V. V. Brus, S. J. Ko, J. Lee, A. Karki, D. X. Cao, K. Cho, G. C. Bazan and T. Q. Nguyen, *Adv. Energy Mater.*, 2019, **9**, 1901438.
96 D. Bartesaghi, I. D. C. Pérez, J. Kniepert, S. Roland, M. Turbiez, D. Neher and L. J. A. Koster, *Nat. Commun.*, 2015, **6**, 1–10.
97 Y. Wang, D. Qian, Y. Cui, H. Zhang, J. Hou, K. Vandewal, T. Kirchartz and F. Gao, *Adv. Energy Mater.*, 2018, **8**, 1801352.
98 S. Yang, Z. Chen, J. Zhu, D. Yang, H. Wang, P. Ding, J. Wu, P. Yan, L. Xie, F. Chen, Y. Wang, J. Zhang and Z. Ge, *Adv. Mater.*, 2024, **36**, 2401789.
99 D. Qian, Z. Zheng, H. Yao, W. Tress, T. R. Hopper, S. Chen, S. Li, J. Liu, S. Chen, J. Zhang, X. K. Liu, B. Gao, L. Ouyang, Y. Jin, G. Pozina, I. A. Buyanova, W. M. Chen, O. Inganäs, V. Coropceanu, J. L. Bredas, H. Yan, J. Hou, F. Zhang, A. A. Bakulin and F. Gao, *Nat. Mater.*, 2018, **17**, 703–709.
100 J. Yao, T. Kirchartz, M. S. Vezie, M. A. Faist, W. Gong, Z. He, H. Wu, J. Troughton, T. Watson and D. Bryant, *Phys. Rev. Appl.*, 2015, **4**, 014020.
101 T. Yang, C. Liao, Y. Duan, X. Xu, M. Deng, L. Yu, R. Li, Q. Peng, T. Yang, C. Liao, X. Xu, M. Deng, L. Yu, Q. Peng, Y. Duan and R. Li, *Adv. Funct. Mater.*, 2022, **32**, 2208950.
102 G. Garcia-Belmonte, A. Munar, E. M. Barea, J. Bisquert, I. Ugarte and R. Pacios, *Org. Electron.*, 2008, **9**, 847–851.
103 E. Von Hauff, *J. Phys. Chem. C*, 2019, **123**, 11329–11346.
104 E. P. Yao, C. C. Chen, J. Gao, Y. Liu, Q. Chen, M. Cai, W. C. Hsu, Z. Hong, G. Li and Y. Yang, *Sol. Energy Mater. Sol. Cells*, 2014, **130**, 20–26.
105 Y. Lin, A. Magomedov, Y. Firdaus, D. Kaltsas, A. El-Labban, H. Faber, D. R. Naphade, E. Yengel, X. Zheng, E. Yarali, N. Chaturvedi, K. Loganathan, D. Gkeka, S. H. AlShammari, O. M. Bakr, F. Laquai, L. Tsetseris, V. Getautis and T. D. Anthopoulos, *ChemSusChem*, 2021, **14**, 3569–3578.
106 S. Braun, W. R. Salaneck and M. Fahlman, *Adv. Mater.*, 2009, **21**, 1450–1472.
107 A. C. Hurd, A. Alotaibi, A. Patterson, O. Alqahtani, J. Doyle, B. Akira, A. C. Authors Ally Hurd and B. Akira Collins, *Mac. J. Phys. Astron.*, 2024, **12**, 9.
108 C. M. Proctor, M. Kuik and T. Q. Nguyen, *Prog. Polym. Sci.*, 2013, **38**, 1941–1960.
109 J. C. Nolasco, A. Castro-Carranza, Y. A. León, C. Brioneş-Jurado, J. Gutowski, J. Parisi and E. von Hauff, *Sol. Energy*, 2019, **184**, 610–619.
110 T. Kirchartz, W. Gong, S. A. Hawks, T. Agostinelli, R. C. I. MacKenzie, Y. Yang and J. Nelson, *J. Phys. Chem. C*, 2012, **116**, 7672–7680.
111 T. Schiros, G. Kladnik, D. Prezzi, A. Ferretti, G. Olivieri, A. Cossaro, L. Floreano, A. Verdini, C. Schenck, M. Cox, A. A. Gorodetsky, K. Plunkett, D. Delongchamp, C. Nuckolls, A. Morgante, D. Cvetko and I. Kymissis, *Adv. Energy Mater.*, 2013, **3**, 894–902.
112 C. J. Brabec, A. Cravino, D. Meissner, N. Serdar Sariciftci, T. Fromherz, M. T. Rispens, L. Sanchez and J. C. Hummelen, *Adv. Funct. Mater.*, 2001, **11**, 374–380.
113 A. A. A. Torimtubun, M. Méndez, E. Moustafa, J. Pallarès, E. Palomares and L. F. Marsal, *Solar RRL*, 2023, **7**, 2300228.
114 W. S. Koh, M. Pant, Y. A. Akimov, W. P. Goh and Y. Li, *IEEE J. Photovolt.*, 2011, **1**, 84–92.
115 J. Larsson, *Am. J. Phys.*, 2007, **75**, 230–239.
116 M. Stephen, K. Genevičius, G. Juška, K. Arlauskas and R. C. Hiorns, *Polym. Int.*, 2017, **66**, 13–25.
117 M. Neukom, S. Züfle, S. Jenatsch and B. Ruhstaller, *Sci. Technol. Adv. Mater.*, 2018, **19**, 291–316.
118 J. Kočka, K. Arlauskas and M. Viliūnas, *Phys. Rev. Lett.*, 2000, **84**, 4946.
119 W. R. Mateker, M. D. McGehee, W. R. Mateker and M. D. McGehee, *Adv. Mater.*, 2017, **28**, 1603940.
120 T. Kumari, I. Vyalih, M. Á. León Luna, H. Ahmed, M. Ahmad, R. Atajanov, E. Jayaraman, S. Manikandan,

B. Paci, A. Di Carlo, J. W. Andreasen, V. Turkovic and M. Madsen, *Cell Rep. Phys. Sci.*, 2024, **5**, 102027.

121 H. Xu, J. Han, M. Babics, L. Huerta Hernandez, D. Rosas Villalva, M. Sanviti, J. Bertrandie, Y. Zhang, Y. Liu, H. Chen, L. Zhao, J. Troughton, J. Martin, F. Laquai, S. De Wolf and D. Baran, *Nat. Photonics*, 2025, **19**, 415–425.

122 Z. Ge, J. Qiao, Y. Li, J. Song, X. Duan, Z. Fu, H. Hu, R. Yang, H. Yin, X. Hao and Y. Sun, *Angew. Chem., Int. Ed.*, 2025, **64**, e202413309.

123 Y. Wang, J. Luke, A. Privitera, N. Rolland, C. Labanti, G. Londi, V. Lemaur, D. T. W. Toolan, A. J. Sneyd, S. Jeong, D. Qian, Y. Olivier, L. Sorace, J. S. Kim, D. Beljonne, Z. Li and A. J. Gillett, *Joule*, 2023, **7**, 810–829.

124 D. E. Shen, A. W. Lang, G. S. Collier, A. M. Österholm, E. M. Smith, A. L. Tomlinson and J. R. Reynolds, *Chem. Mater.*, 2022, **34**, 1041–1051.

125 H. Chen, Y. Huang, R. Zhang, H. Mou, J. Ding, J. Zhou, Z. Wang, H. Li, W. Chen, J. Zhu, Q. Cheng, H. Gu, X. Wu, T. Zhang, Y. Wang, H. Zhu, Z. Xie, F. Gao, Y. Li and Y. Li, *Nat. Mater.*, 2025, **24**, 444–453.

126 T. Hanabusa, K. Kusaka and O. Sakata, *Thin Solid Films*, 2004, **459**, 245–248.

